Supplementary Information

Demystifying Constructive Strategies on Designing Functionalized Lamellar Nb_2CTx Nanosheet Membrane Architectures under Confined Space

*Wenjihao Hu[a,b], Lei Xie[b,c], Chenyang Zhang[c], Jingyi Wang[b], Chenyu Qiao[b], Sijia Li[b], Jingsi Chen[b], Ziqian Zhao[b] and Hongbo Zeng[b]**

a. *School of Metallurgy & Environment and Chinese National Engineering Research Center for Control & Treatment of Heavy Metal Pollution, Central South University, Changsha, Hunan, 410083, China*
b. *Department of Chemical and Materials Engineering, University of Alberta, Edmonton, AB, T6G 1H9, Canada*
c. *School of the Resources Processing and Bioengineering, Central South University, Changsha 410083, China*

Corresponding author. E-mail: hongbo.zeng@ualberta.ca , Phone: 780-492-1044, Fax: 780-492-2881

Methods

Materials

All chemicals and materials were used as received. Poly(acrylic acid) (25 wt% solution in water, Alfa Aesar), Poly(vinyl alcohol) (Mw: 31,000-50,000, 98-99% hydrolyzed, Sigma Aldrich) and Gallic acid (anhydrous, Mw 170.12 g/mol, Sigma Aldrich) were used as surface modifier. 11-Mercaptoundecanoic acid (assay: 95%, Mw: 218.36 g/mol, mp: 46-50 ^{0}C (lit.)) and 11-Mercapto-1-undecanol (assay: 97%, Mw: 204.37 g/mol, mp: 33-37 ^{0}C (lit), fp: > 113 ^{0}C closed cup) were used as -COOH and -OH modeling molecules. Bulk Nb_2AlC (purity: 98%, particle size: 38 μm, -400 mesh) was purchased from Weina Scientific (Shanghai) co. Ltd. Hydrofluoric Acid (49 wt%) was used as ethcing agent. Ethanol (max 0.01% H_2O, CAS No. 64-17-5, EC Number 200-578-6, Sigma Aldrich) was used as dispersant and washing reagent after etching process. Dimethylsulfoxide (DMSO, >99.7 wt.%, Sigma Aldrich) was the polar solvent for delamination process. Porous polyvinylidene fluoride (PVDF) (47 mm diameter, 0.22 μm pore size, Fisher Scientific) was the membrane substrate.

Characterization

Transmission electron microscopy (TEM) (JEOL, JEM-ARM200CF S/TEM (Narwhal)) was operated at 200 kV. Atomic force microscopy (AFM) was employed for topographic imaging and force mapping (Asylum MFP-3D AFM). X-ray diffraction (XRD) (Rigaku XRD Ultima IV) was in a diffraction system with 40 kV and 44 mA, and the scanning angle was 5^0 to 80^0. Scanning electron microscopy (SEM) (Zeiss Sigma Field Emission) with energy dispersive X-ray spectroscopy (EDX) (Bruker, dual silicon drift detectors, each with an area of 60 mm^2 and a resolution of 123 eV) mapping was performed with a high resolution of ~10 nm. The X-ray

photoelectron spectroscopy (XPS) (Kratos AXIS Ultra) and Fourier-transform infrared spectroscopy (FTIR) (Thermo Fisher Scientific using attenuated total reflection (ATR) mode) were used as material characterization. UV-2000 spectrophotometer was used in quartz cuvettes with a path length of 2 mm. Inductive Coupled Plasma (ICP) Emission Spectrometer was used as ion detection.

Nb_2CTx MXene nanosheets

The Nb_2AlC (purity: 98%, particle size: 38 μm, -400 mesh) was directly purchased from Weina Scientific (Shanghai) co. Ltd. 1.032 g Nb_2AlC powder was weighted and immersed in 50 mL Hydrofluoric Acid (49 wt%) with 200 rpm magnetic stirring in a Teflon container at room temperature for 72 h. The suspension was rinsed by ethanol followed by centrifugation process (Eppendorf 5430) for 10 minutes (5000 rpm) named as washing step in order to remove hydrofluoric acid from the suspension. The washing step took several times for the complete removal of hydrofluoric acid from the suspension. The remaining sediment after the washing step was prepared for the delamination process.

Delamination of Nb_2CTx MXene nanosheets

The delamination process was performed by intercalating the Nb_2CTx nanosheets using polar solvent Dimethyl sulfoxide (DMSO, >99.7 wt%, Sigma Aldrich) under room temperature, after which the suspension was centrifuged to separate the multilayered Nb_2CTx MXene nanosheet sediments from the polar solvent. The resulting sediment was dried and dispersed in water for storage at room temperature.

Synthesis of Nb_2CTx-PAA, Nb_2CTx-PVA, and Nb_2CTx-GA nanosheets suspension

The Nb_2CT_x MXene nanosheets suspension (2 mg/ml) was mixed with 1 mg/ml Poly(acrylic acid) solution (Nb_2CTx-PAA), Poly(vinyl alcohol) solution (Nb_2CTx-PVA) and Gallic acid (Nb_2CTx-GA) at a weight ratio of 1:1. The above three suspensions were placed under ultrasonication process for 24 h to make a homogeneous surface modification of Nb_2CTx MXene nanosheets.

Synthesis of Nb_2CTx-PAA, Nb_2CTx-PVA, and Nb_2CTx-GA nanosheets membrane

The well mixed Nb_2CTx-PAA, Nb_2CTx-PVA, and Nb_2CTx-GA suspension were filtered through Polyvinylidene fluoride (PVDF) membranes (0.22 μm, 47 mm in diameter, ~0.7 bar) under vacuum. The filtered Nb_2CTx-PAA, Nb_2CTx-PVA, and Nb_2CTx-GA membranes were then dried under room temperature for three days.

Nb_2CTx-PAA, Nb_2CTx-PVA, and Nb_2CTx-GA nanosheets membrane testing condition

LiCl and $MgCl_2$ were the salt solutions for testing water flux and cation rejection under osmotic static diffusion. The feed side was 200 ml DI water and the draw side was 0.25 M salt solution under room temperature and pressure. The cation concentration was tested by using ICP Emission Spectrometer. The driving force was only the osmotic pressure.

Osmotic pressure

The forward osmotic pressure attributed to the concentration difference between feed side and draw side was calculated by using Vant Hoff equation

$$\Pi = CRT \quad (1)$$

where Π is the osmotic pressure in atm (1 atm = 1.01325 bar), C is the concentration gradient across the membrane in g/mole, R is the universal constant 0.0821 atm*L/mole*K or 0.08314

L*bar*K^{-1}*$mole^{-1}$, and T is the temperature in K. The osmotic pressure gradually decreases due to the water transport from feed side to draw side.

Water transport rate

The rate of water permeation through the semipermeable membrane is defined as:

$$J_w = \frac{\Delta V}{S \times h} \tag{2}$$

where J_w is the water permeation rate in LMH, ΔV is the volume change for water after osmotic pressure static diffusion process at steady state, h is the steady state diffusion time, and S is the effective area of membrane. During water transport process from feed side to draw side, a reverse transport for ions might occur.

Ion transport rate

The cation permeation through the membrane was defined as

$$J_s = \frac{(C_t V_t - C_0 V_0)}{S \times h} \tag{3}$$

where J_s is the flow rate of cation through the membrane, C_0, V_0 are the feed concentration and volume at time 0 and C_t, V_t indicate the final salt concentration and feed volume over time, h is the steady state diffusion time, and S is the effective area of membrane.

Charge interactions from Coulomb's Law

The salts dissolving in water would result in charged ions which obey coulomb's law. The oppositely charged ions would have either attractive or repulsive interactions within the confined

channel of the membrane. In this work, the coulombic attraction between cations (e.g. Li^+ and Mg^{2+}) and anions (e.g. Cl^-) can be calculated using

$$W(r) = \frac{z_1 z_2 e^2}{4\pi\varepsilon_0 \varepsilon r} \quad (4)$$

Where z_1, z_2 are the valency of cations and anions; e is the charge of electron ($e = 1.602 \times 10^{-19}$ C); ε_0 is the permittivity in vacuum (8.85×10^{-12} F m^{-1}); ε is the dielectric constant of LiCl (ε = 11.05) and $MgCl_2$ (ε = 69.605) solution in water (at 20 ^{0}C); r is separation distance for cation and anion in (m) (Supplementary Table 1)[1].

A useful quantity called the *Bjerrum length* l_B, was defined as the charge separation at which the coulomb energy u (r) between a mole of ion pairs just equals the thermal energy RT[2].

$$l_B = \frac{e^2 N_A}{4\Pi\varepsilon_0 \varepsilon RT} \quad (5)$$

Where e is the charge of electron ($e = 1.602 \times 10^{-19}$ C); N_A is the Avogadro constant (6.022×10^{23} molecule mol^{-1}); ε_0 is the permittivity in vacuum (8.85×10^{-12} F m^{-1}); ε is the dielectric constant of LiCl (ε = 11.05) and $MgCl_2$ (ε = 69.605) solution in water (at 20 ^{0}C); R is gas constant (R = 8.314J/mol); T is the temperature (T = 293.15 K).

General Gibbs reaction energy (formation energy)

The salt solution could cluster together into stable structures within confined channels inside the membrane. The positively charged atomic nuclei would form covalent bonds with the surrounded negatively charged electron density[2]. The atomic nuclei "glue" together with the surrounded negatively charged electrons result in the possible formation of ion cluster through electrostatic bonding[3]. The process could be understood using thermodynamic energy equation

$$\Delta G' = C\,\Delta U + C\,\gamma_{SAL} \tag{6}$$

Where ΔG' is the formation energy of ion cluster (kcal); C is the total concentration of salt solution (M); ΔU is the pairwise energy for the ion cluster (kcal mol^{-1}); the pairwise energy could be calculated using Madelung constant M (Supplementary Table 2)[3]

$$\Delta U = -M\,\frac{e^2 N_A}{4\Pi\varepsilon_0 r} \tag{7}$$

Where e is the charge of electron (e = 1.602 × 10^{-19} C); ε_0 is the permittivity in vacuum (8.85 × 10^{-12} F m^{-1}); r is distance for separating cation and anion in (m) (Supplementary Table 1)[1]; N_A is the Avogadro constant (6.022 × 10^{23} molecule mol^{-1}); the first term of Eq. 6 represents the cohesive or binding energy of an ion pair, and the second term of Eq. 6 is the solvation energy of salts in water.

The ion solvation could be calculated by using the Gibbs-Helmholtz equation[2]

$$\Delta\gamma_{SAL} = \Delta G_{el} - T\frac{d\Delta G_{el}}{dT} \tag{8}$$

ΔG_{el} represents the free energy in the medium with dielectric constant (ε) for the salt solution.

$$\Delta G_{el} = \frac{-q^2}{8\Pi\varepsilon\varepsilon_0 r} \tag{9}$$

Eq. 8 would then become

$$\Delta\gamma_{SAL} = -\frac{q^2}{8\Pi\varepsilon_0 r}\left(1 - \frac{1}{\varepsilon} - \frac{1}{\varepsilon}\frac{d\ln\varepsilon}{d\ln T}\right) \tag{10}$$

Where ε is the dielectric constant of LiCl (ε = 11.05) and $MgCl_2$ (ε = 69.605) solution in water (at 20 ^{0}C); ε_0 is the permittivity in vacuum (8.85×10^{-12} F m^{-1}); T is the temperature (T = 293.15 K); q is the magnitude of charge.

Computational methods

The first principal calculations were performed by using Revision D.01 of Gaussian 09[3] to demonstrate the geometric and electronic structures of Li^+ (Mg^{2+}) cluster with Cl^- and water molecules. Specifically, the B3LYP combination of exchange and correlation functionals with the aug-cc-pvdz basis set was adopted in these calculations[4], which could provide reasonable structures and energetic results for a variety of late transition metal aqueous systems[5]. The initial geometries of geometry optimizations were constructed based upon idealized structures from ligand field theory and thermochemistry calculations using a tight SCF energy convergence of 10^{-8} and an ultrafine grid for numerical integration. The formation reaction energies of Li^+ (Mg^{2+}) clusters were obtained by the following equation:

$$\Delta G_f = G(A_m B_n) - m \times G(A) - n \times G(B) \quad (11)$$

Lattice Boltzmann Method

The flow in membranes was simplified and simulated with the Lattice Boltzmann Method (LBM). The LBM described the motion of ionic solution in membranes by conducting the collision and transition of particles (molecular aggregation) on the mesh, during which the membrane was considered as porous boundaries, while the interactions between groups on membranes and ions were expressed as motivation and resistance to particles' motion. Finally, the solution flowrate passing through the membrane can be determined by the statistic data of particle distribution, which coincides well with experimental results.

The Lattice Boltzmann Method was employed to describe the flow of ionic solution through the membrane. This method is based on molecular dynamics, simulating transport phenomena by conducting the collision and transition of particles (molecular aggregation) on mesh models. In this work, the flow process was simplified as a 2D model, in which the multi-laminar membrane was considered as several porous boundaries. The simulation was conducted with D2Q9 format, of which the total time steps are 40,000, standing for 80 s. At each step, particles at the same node collide with another one with opposite velocities to update their velocities (Eq. 12). This process shows the change of flow rate in the membrane. Then, particles transfer on the mesh model according to their new velocities, which represents the movement of solution (Eq. 13). It is worth noting that, the particles moving to boundaries are given opposite velocities according to the rule of bounce back boundary, which represents the resistance induced by membrane on solution movement. In this way, the flowrate through the membrane can be determined with statistic data of particle distribution (Eq. 14), which coincides well with experimental results.

$$f_i(x,y,t) = (1-\omega_{\mathrm{f}}) \cdot f_i(x,y,t) + \omega_{\mathrm{f}} \cdot f_i^{\mathrm{eq}}(x,y,t) \tag{12}$$

$$f_i(x+\Delta x, y+\Delta y, t+\Delta t) = f_i(x,y,t) \tag{13}$$

$$f_i^{\mathrm{eq}}(x,y,t) = \varpi_i \overline{c}(x,y,t) \tag{14}$$

Where f_i and f_i^{eq} are molecule distribution equation for real-time and under equilibrium state, respectively; i is the index of velocity of particles, 1-9 for D2Q9 format; ω_f is the relaxation frequency; ϖ_i is the weight for particle with velocity i, which is constant for D2Q9 format.

Supplementary Table 1. Hydrated radii and hydration numbers of ions in water (Approximate)[1]

Ion	Bare ion radius (nm)	Hydrated radius (nm)	Hydration number (±1)	Lifetime/exchange rate (s)
Li^+	0.068	0.38	5	5×10^{-9}
Mg^{2+}	0.065	0.43	6	10^{-6}
OH^-	0.176	0.30	3	NA
Cl^-	0.181	0.33	1	$\sim 10^{-11}$

Supplementary Table 2. Madelung's constant[4,5]

Madelung's constant		
Ion	Mole	Crystal lattice
LiCl	1.748	Octahedral
$MgCl_2$	4.472	Octahedral

Supplementary Table 3. Formation energy of ion in water

Ion	ΔU （kcal/mole）	γ_{sal}（kcal/mole）	Δ G' (kcal/mole)
LiCl	-232.55	48.7	-45.97
$MgCl_2$	-602.21	308.74	-73.37

Supplementary Table 4. Computational calculation

Cluster	ΔG(kcal/mol)
$[LiCl_2]^-$	-194.9
$[MgCl_4]^{2-}$	-418.6
LiCl	-146.7
$[MgCl]^+$	-591.8
$[LiH_2O]^+$	-26.8
$[MgH_2O]^{2+}$	-334.3
Li_4Cl_4	-694.0
Mg_6Cl_{12}	-4844.2
$[Li(6H_2O)]^-$	-61.2
$[Mg(6H_2O)]^{2+}$	-511.4

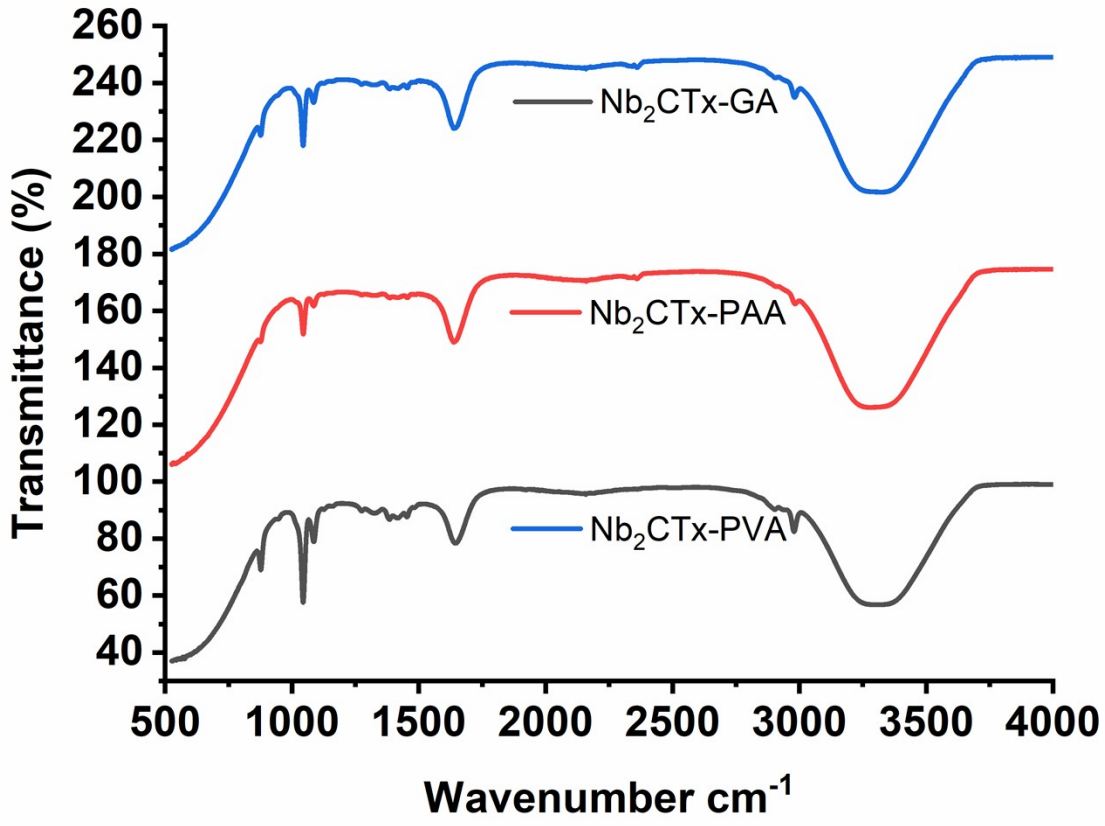

Fig. S1. ATR-FTIR spectra of Nb_2CTx-PVA, Nb_2CTx-PAA and Nb_2CTx-GA nanosheets.

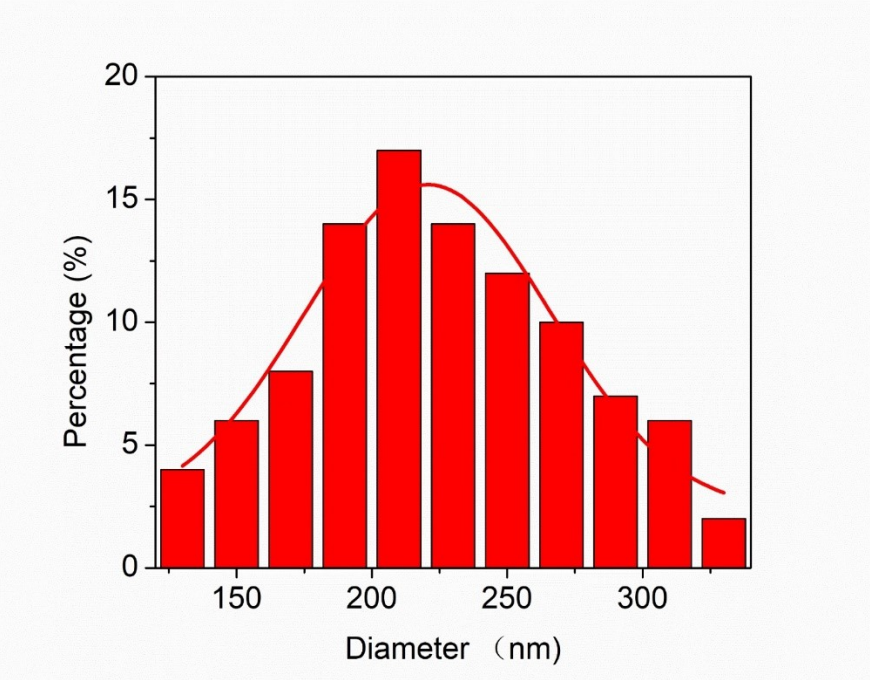

Fig. S2. Laminar size distribution of Nb_2CTx MXene nanosheets.

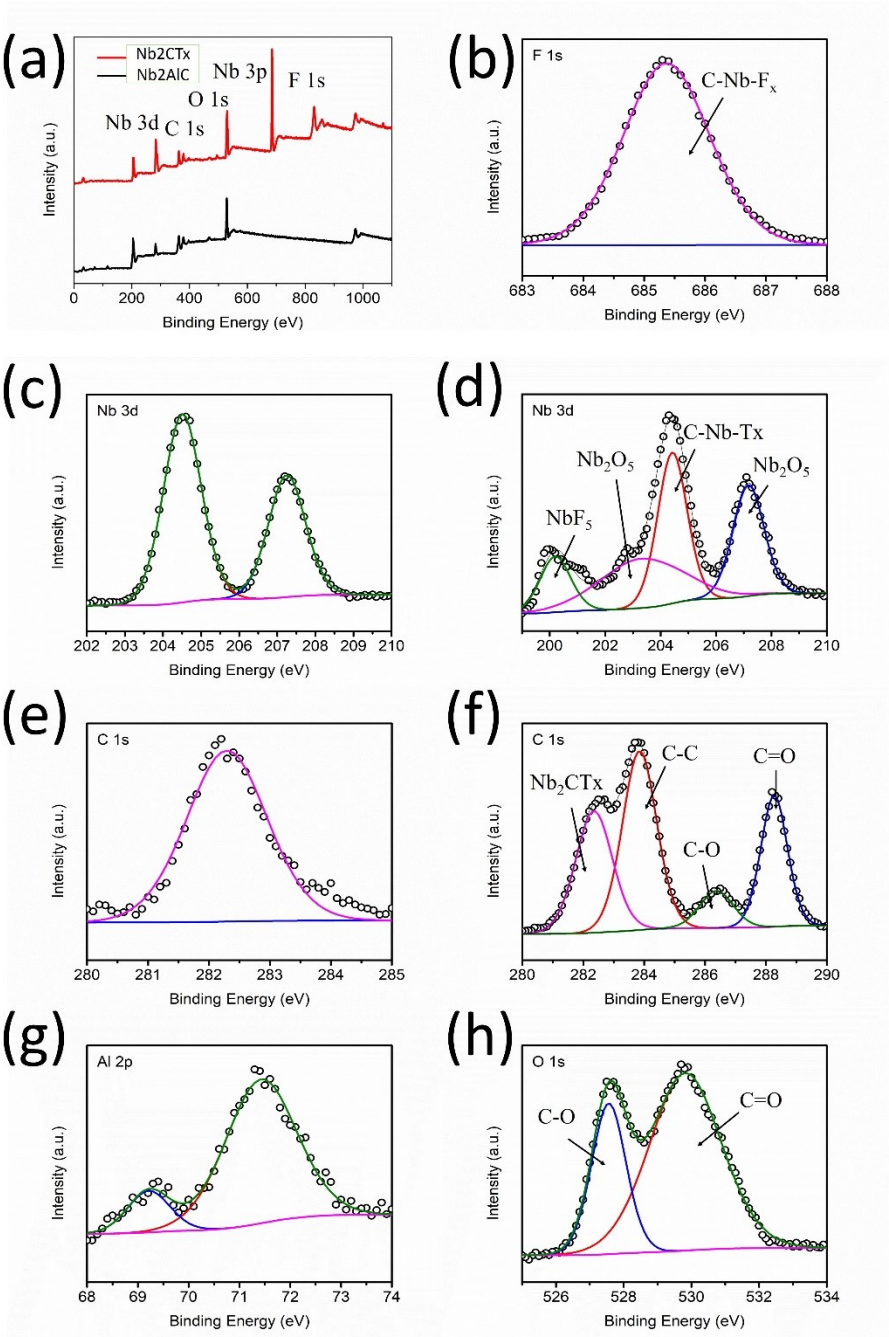

Fig. S3. XPS spectra of Nb_2AlC powders and Nb_2CTx MXene nanosheets. (a) XPS full spectra of Nb_2AlC powders and Nb_2CTx MXene nanosheets. (b) High resolution F1s XPS spectrum for Nb_2CTx MXene nanosheets. (c) High resolution Nb3d XPS spectrum for Nb_2AlC powders and (d) Nb_2CTx MXene nanosheets. (e) High resolution C 1s XPS spectrum for Nb_2AlC powders and (f) Nb_2CTx MXene nanosheets. (g) High resolution Al 2p XPS spectrum for Nb_2AlC powders. (h) high resolution O 1s XPS spectrum for Nb_2CTx MXene nanosheets.

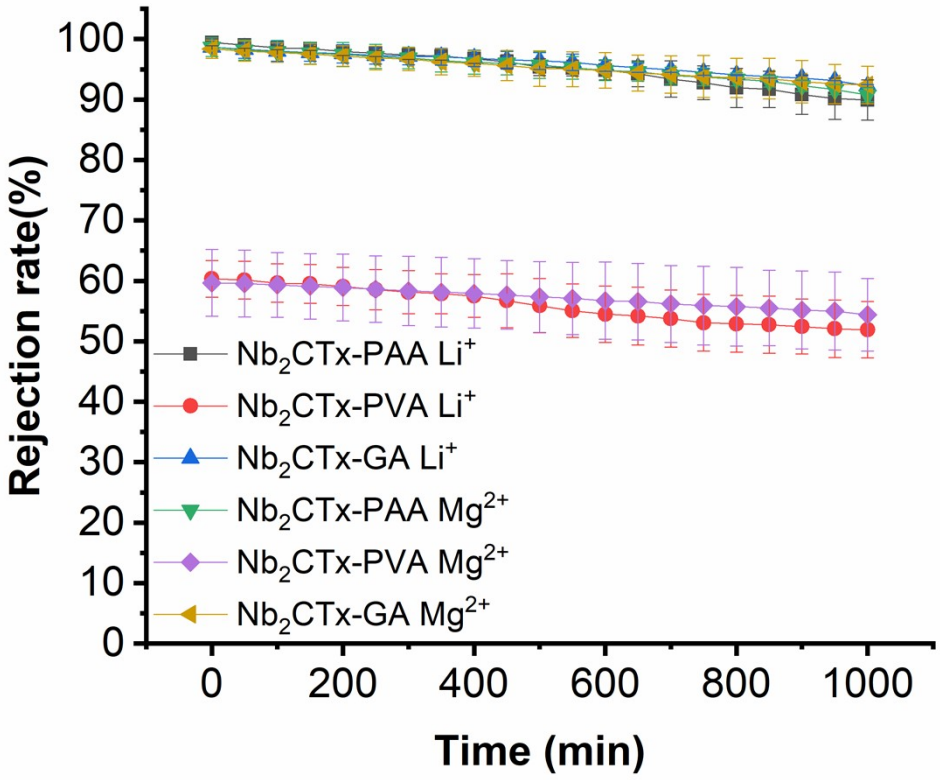

Fig. S4. Long-term ion rejection stability test of Nb_2CTx-PAA, Nb_2CTx-PVA and Nb_2CTx-GA nanosheet membranes.

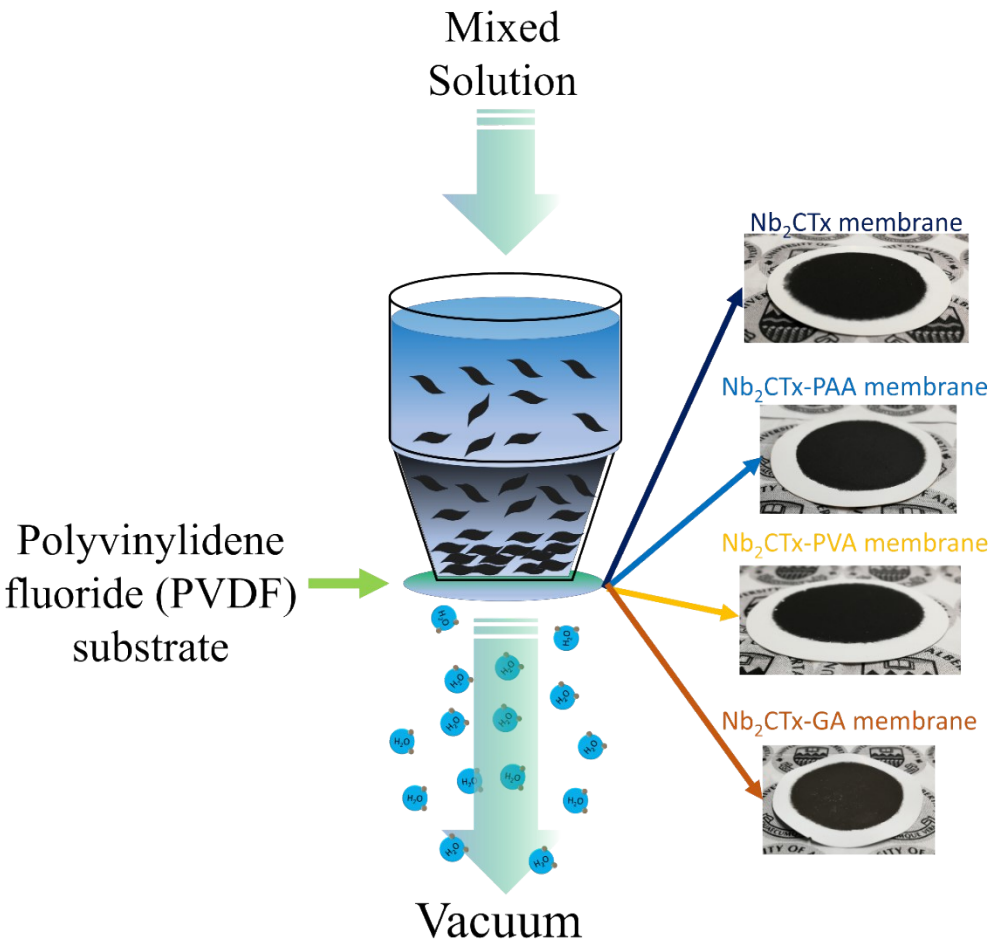

Fig. S5. Schematic illustration for filtration process. Filtration set-up for synthesizing Nb2CTx, Nb2CTx-PAA, Nb2CTx-PVA and Nb2CTx-GA membranes (~0.7 bar vacuum pressure, polyvinylidene fluoride (PVDF) substrate).

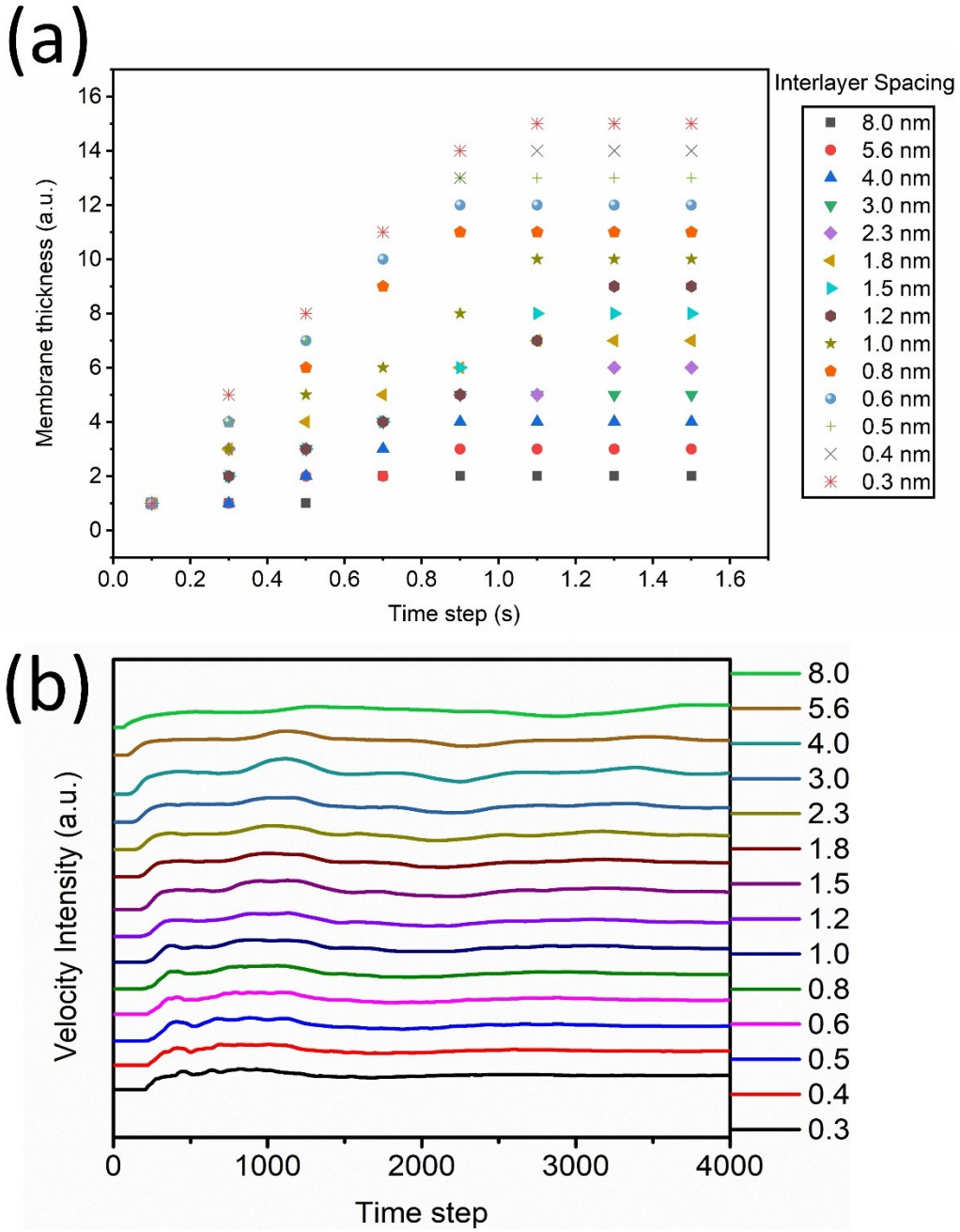

Fig. S6. Simulation results using lattice Boltzmann method. (a) Calculating the water permeation distance varied by interlayer spacing of the model pristine membrane. (b) The output water velocity varied by interlayer spacing of the model pristine membrane (1 step = 2 ms).

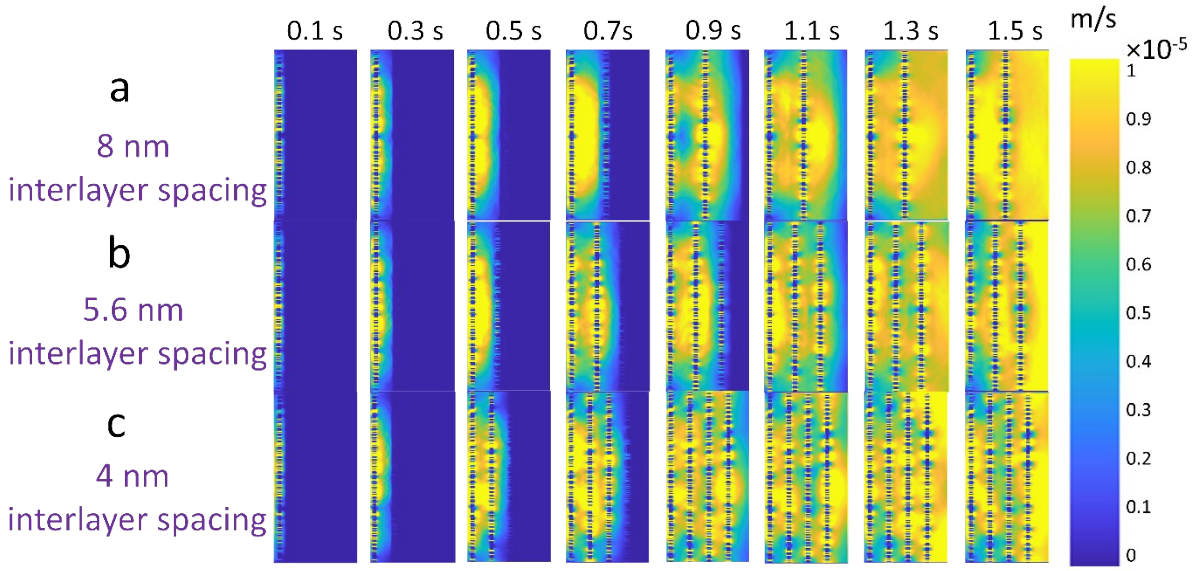

Fig. S7. Simulation results on water permeation within multiple interlayer spacing of membrane by using Lattice Boltzmann method. (a) 8 nm interlayer spacing. (b) 5.6 nm interlayer spacing. (c) 4 nm interlayer spacing. The above membranes have confined thickness (~15 nm) and time step (50, 1step = 2 ms).

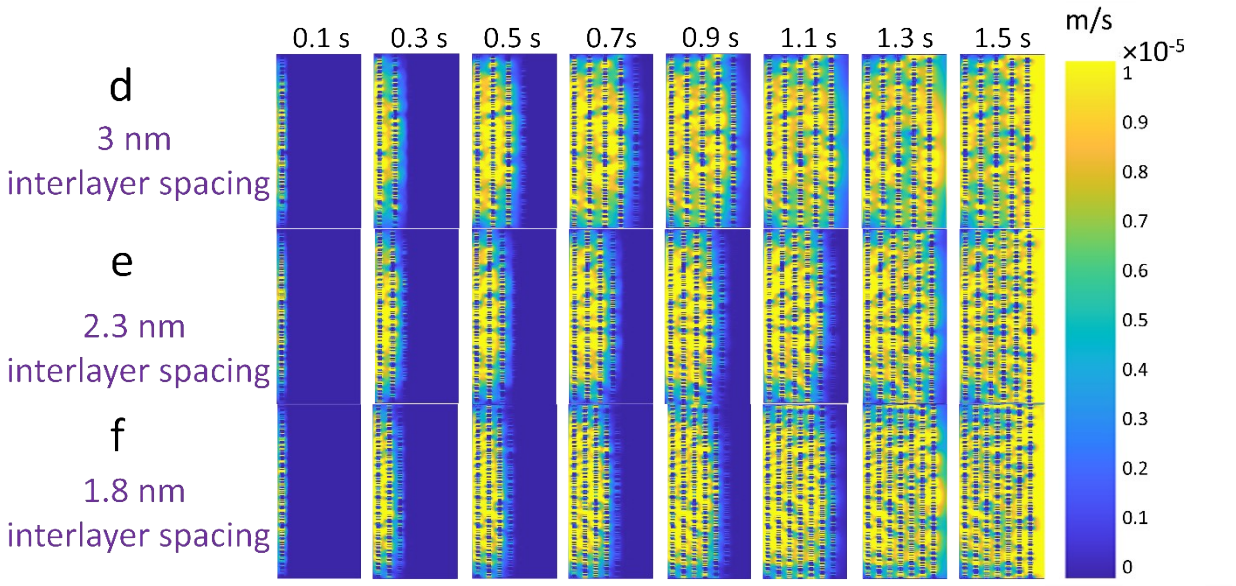

Fig. S8. Simulation results on water permeation within multiple interlayer spacing of membrane by using Lattice Boltzmann method as continued from Fig.S7. (d) 3 nm interlayer spacing. (e) 2.3 nm interlayer spacing. (f) 1.8 nm interlayer spacing. The above membranes have confined thickness (~15 nm) and time step (50, 1step = 2 ms).

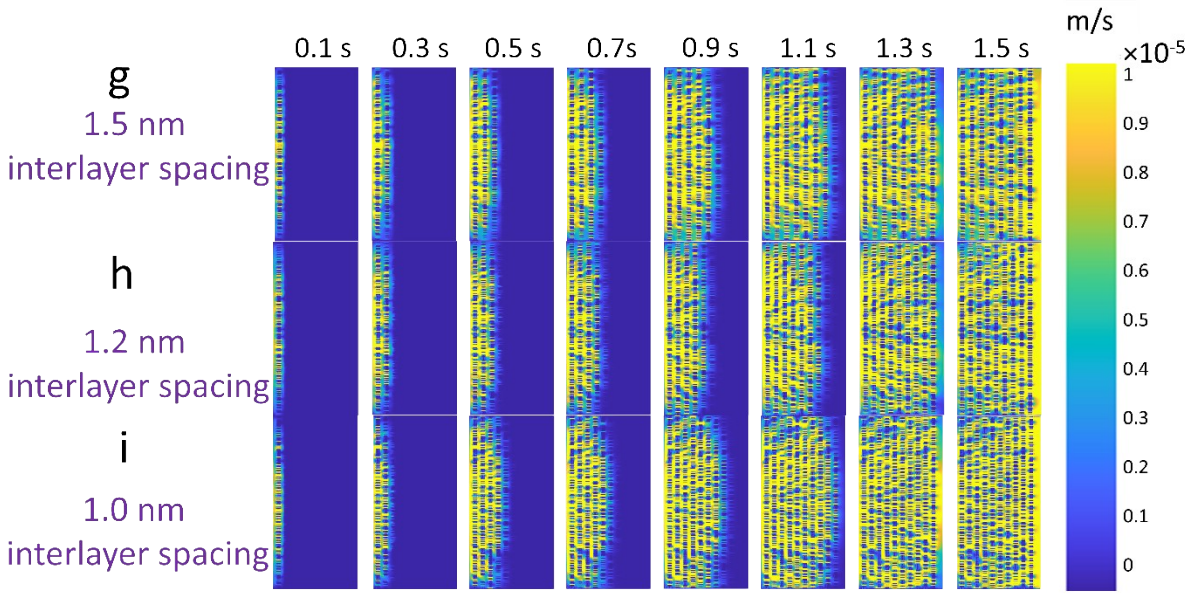

Fig. S9. Simulation results on water permeation within multiple interlayer spacing of membrane by using Lattice Boltzmann method as continued from Fig. S8. (g) 1.5 nm interlayer spacing. (h) 1.2 nm interlayer spacing. (i) 1.0 nm interlayer spacing. The above membranes have confined thickness (~15 nm) and time step (50, 1step = 2 ms).

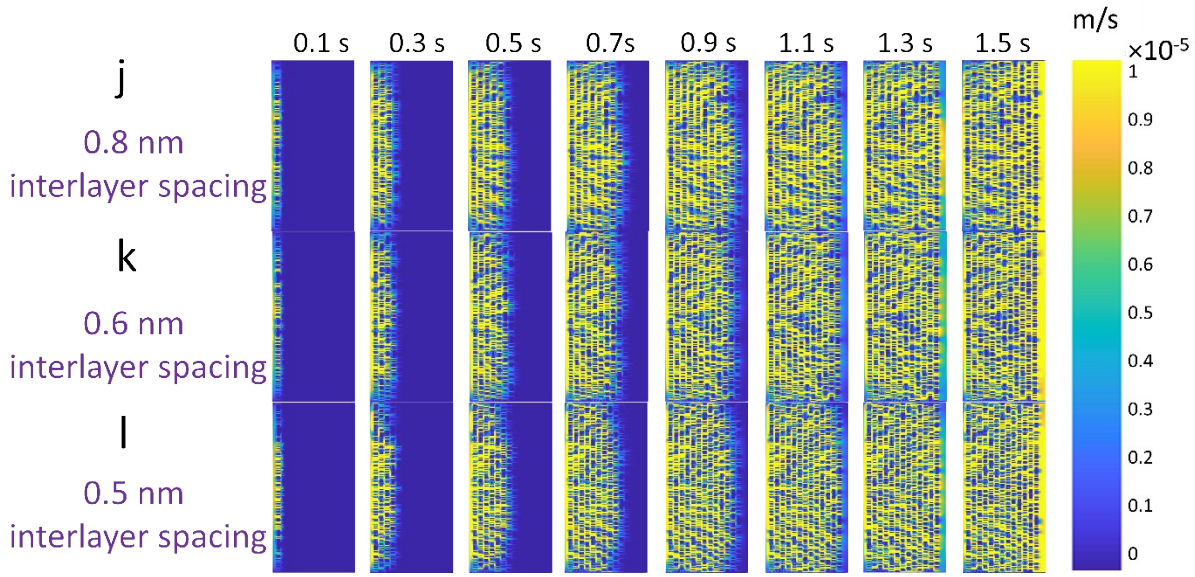

Fig. S10. Simulation results on water permeation within multiple interlayer spacing of membrane by using Lattice Boltzmann method as continued from Fig. S9. (j) 0.8 nm interlayer spacing. (k) 0.6 nm interlayer spacing. (l) 0.5 nm interlayer spacing. The above membranes have confined thickness (~15 nm) and time step (50, 1step = 2 ms).

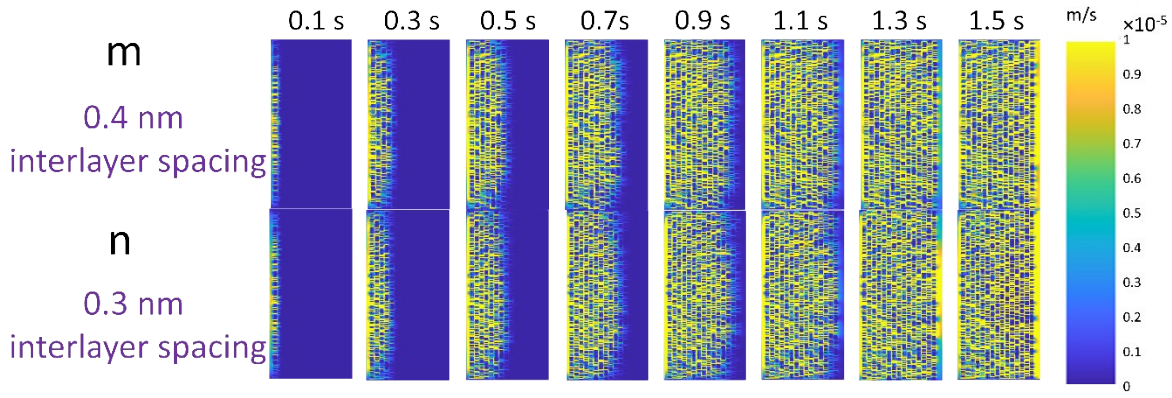

Fig. S11. Simulation results on water permeation within multiple interlayer spacing of membrane by using Lattice Boltzmann method as continued from Fig. S10. (m) 0.4 nm interlayer spacing. (n) 0.3 nm interlayer spacing. The above membranes have confined thickness (~15 nm) and time step (50, 1step = 2 ms).

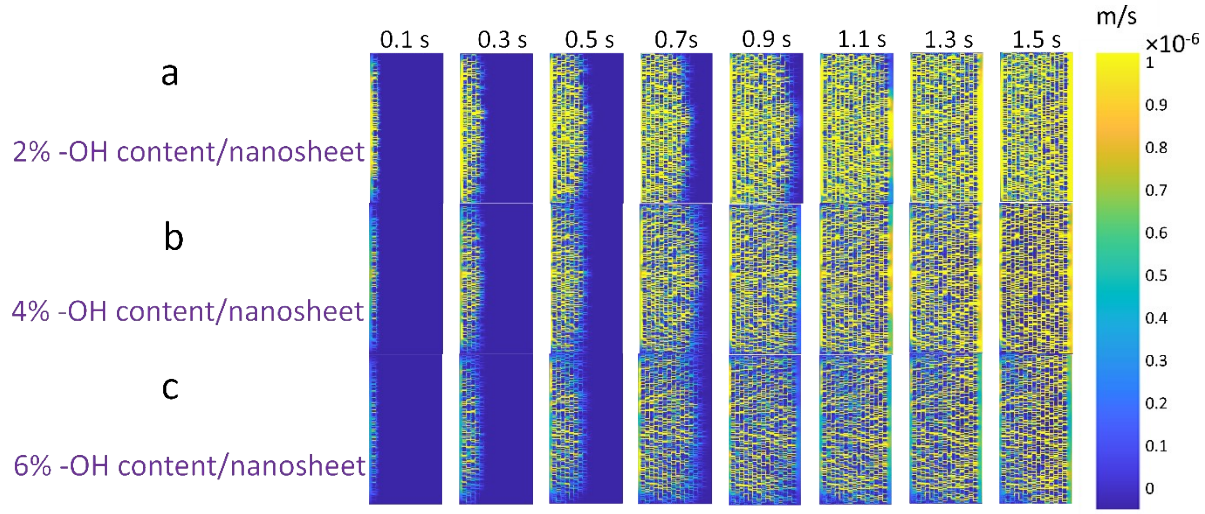

Fig. S12. Simulation results on water permeation within multiple -OH content/nanosheet membrane by using Lattice Boltzmann method as continued from Fig. S11. (a) 2% -OH content/nanosheet. (b) 4% -OH content/nanosheet. (c), 6% -OH content/nanosheet. The above membranes have confined thickness (~200 nm) and time step (50, 1step = 2 ms). The nanosheets are negligible friction loss.

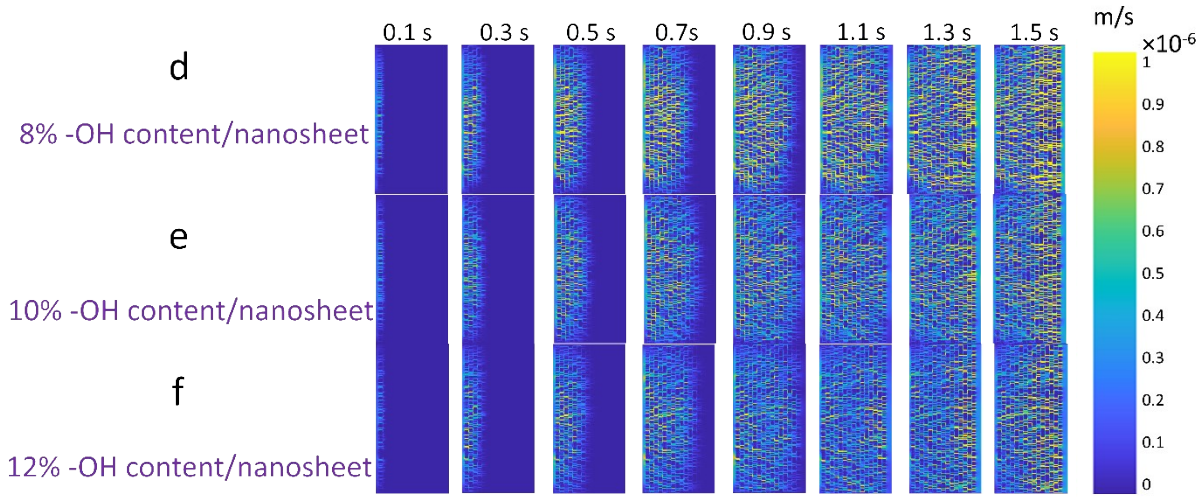

Fig. S13. Simulation results on water permeation within multiple -OH content/nanosheet membrane by using Lattice Boltzmann method as continued from Fig. S12. (d) 8% -OH content/nanosheet. (e) 10% -OH content/nanosheet. (f) 12% -OH content/nanosheet. The above membranes have confined thickness (~200 nm) and time step (50, 1step = 2 ms). The nanosheets are negligible friction loss.

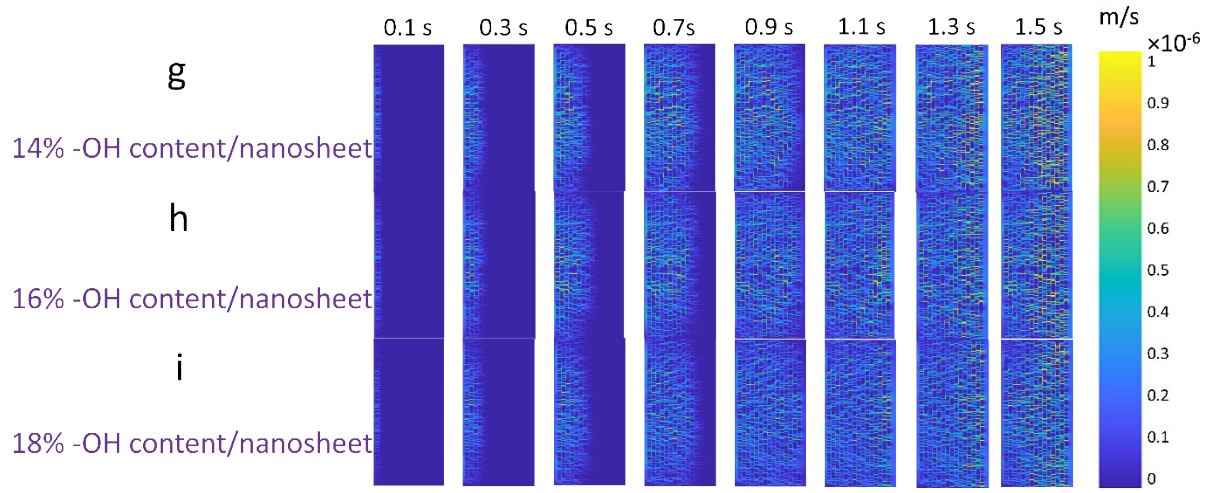

Fig. S14. Simulation results on water permeation within multiple -OH content/nanosheet membrane by using Lattice Boltzmann method as continued from Fig. S13. (g) 14% -OH content/nanosheet. (h) 16% -OH content/nanosheet. (i) 18% -OH content/nanosheet. The above membranes have confined thickness (~200 nm) and time step (50, 1step = 2 ms). The nanosheets are negligible friction loss.

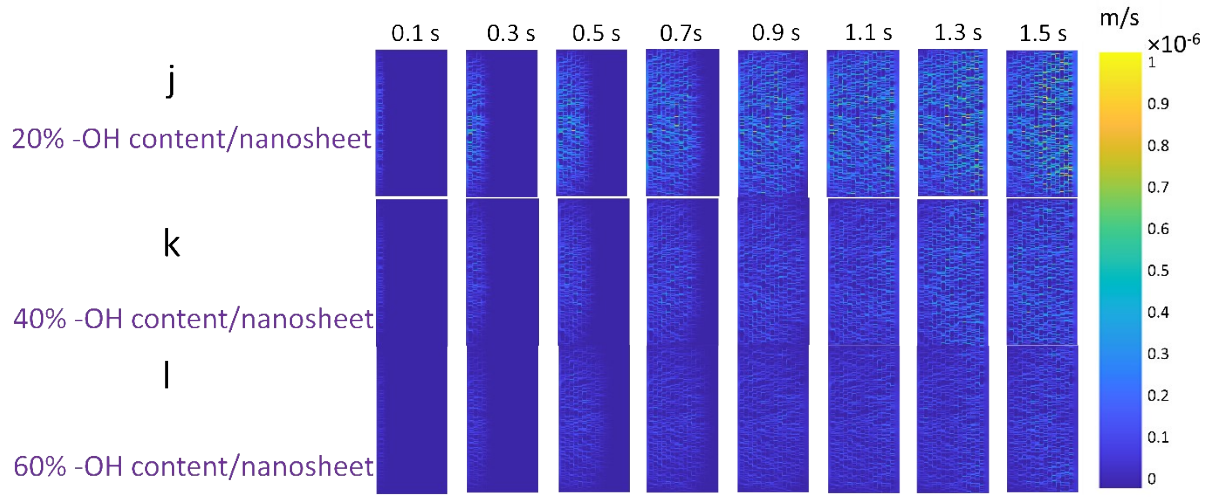

Fig. S15. Simulation results on water permeation within multiple -OH content/nanosheet membrane by using Lattice Boltzmann method as continued from Fig. S14. (j) 20% -OH content/nanosheet. (k) 40% -OH content/nanosheet. (l) 60% -OH content/nanosheet. The above membranes have confined thickness (~200 nm) and time step (50, 1step = 2 ms). The nanosheets are negligible friction loss.

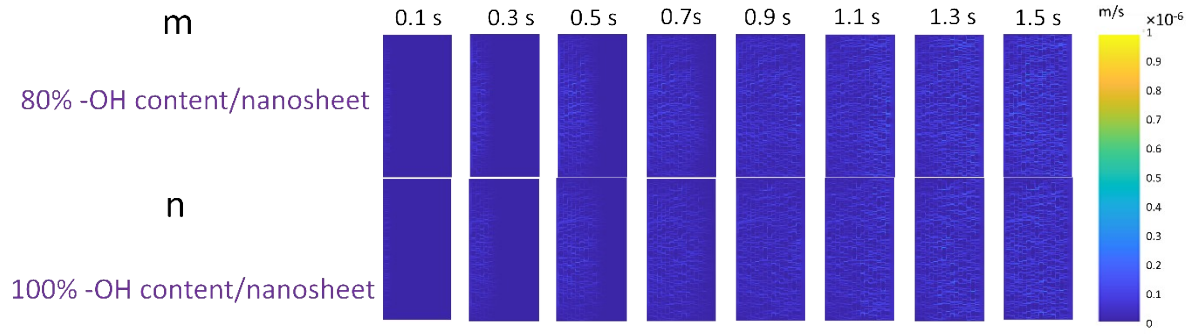

Fig. S16. Simulation results on water permeation within multiple -OH content/nanosheet membrane by using Lattice Boltzmann method as continued from Fig. S15. (m) 80% -OH content/nanosheet. (n) 100% -OH content/nanosheet. The above membranes have confined thickness (~200 nm) and time step (50, 1step = 2 ms). The nanosheets are negligible friction loss.

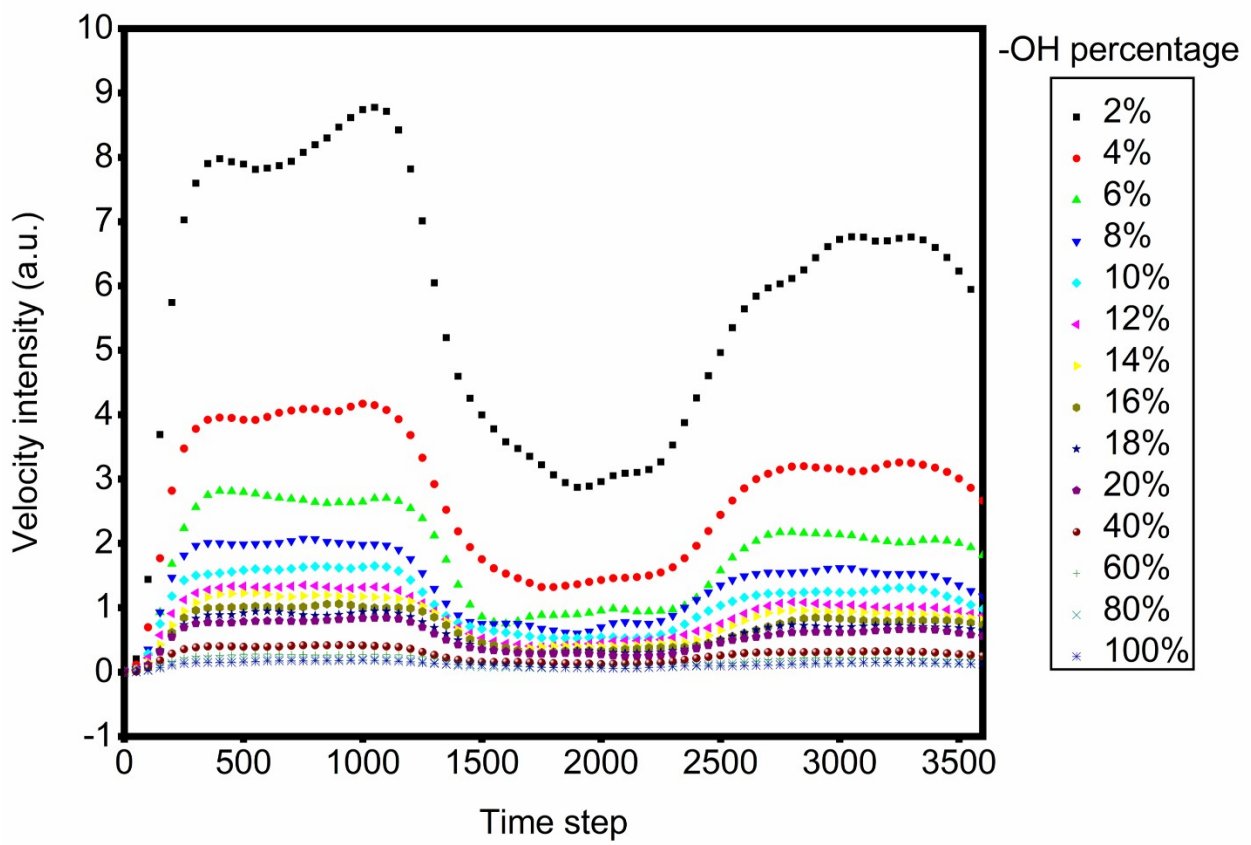

Fig. S17. Simulation results on water permeation velocity within multiple -OH content/nanosheet membrane with longer time steps ~4000 steps by using Lattice Boltzmann method..

Figure S17 shows the simulation results on the water permeation velocity with time within the nanosheet membranes of varying -OH contents. In Figure S17, -OH functional groups represent the obstacles within the internal channel of the nanoconfined 2D channels. At a certain ion concentration, the obstacles limit the nanoconfined space for both free water and ions to pass through. Therefore, the higher content of obstacles, the lower output velocity of water clusters to permeate. From time step 0 to 4000, the output velocity profiles show three regimes, which is governed by the synergistic effect between clusters and upcoming water molecules. The upcoming water molecules inside the nanoconfined 2D channels provide driving force for water clusters to permeate. At the initial stage, the water molecules can be quickly transported within the space, and

reach a maximum level of content (maximum velocity). Then, the water molecules will face upon the obstacles inside the nanochannels, and will be gradually gathered around to form water clusters, which limits their moving speed due to the highly limited space and upcoming water molecules. The driving force would gradually increase with more upcoming water molecules accumulated inside the nanochannels. The whole process would finally be stabilized at a relatively constant velocity level.

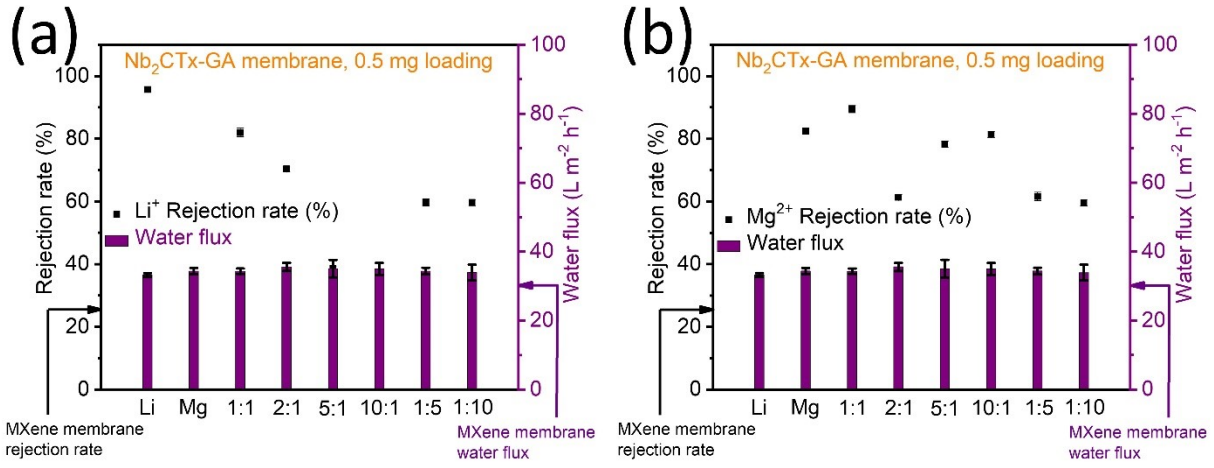

Fig. S18. Results on the selective separation of ions for different ratios using Nb_2CTx-GA nanosheet membrane (with 0.5 mg loading): (a) Li^+ and (b) Mg^{2+}.

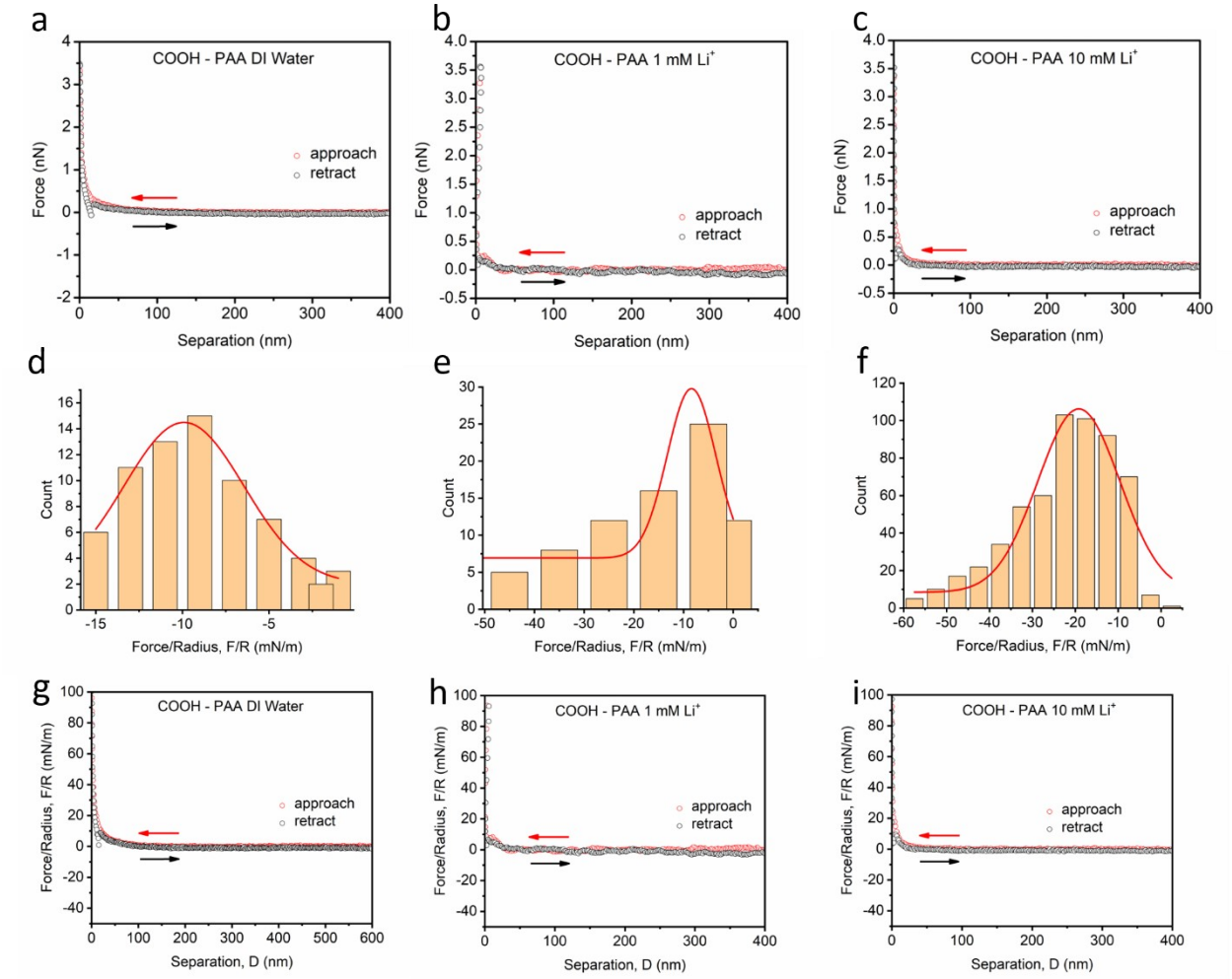

Fig. S19. AFM force measurement between 11-mercaptoundecanoic acid modified tip and Nb_2CTx-PAA covered silica surface in (a) DI water, (b) 1 mM Li^+, and (c) 10 mM Li^+. AFM force mapping distribution histogram for 11-mercaptoundecanoic acid modified tip interacting with Nb_2CTx-PAA covered silica surface in (d) DI water, (e) 1 mM Li^+, and (f) 10 mM Li^+. Normalized interaction force (Force/tip radius ~30 nm) as a function of separation curve in (g) DI water, (h) 1 mM Li^+, and (i) 10 mM Li^+.

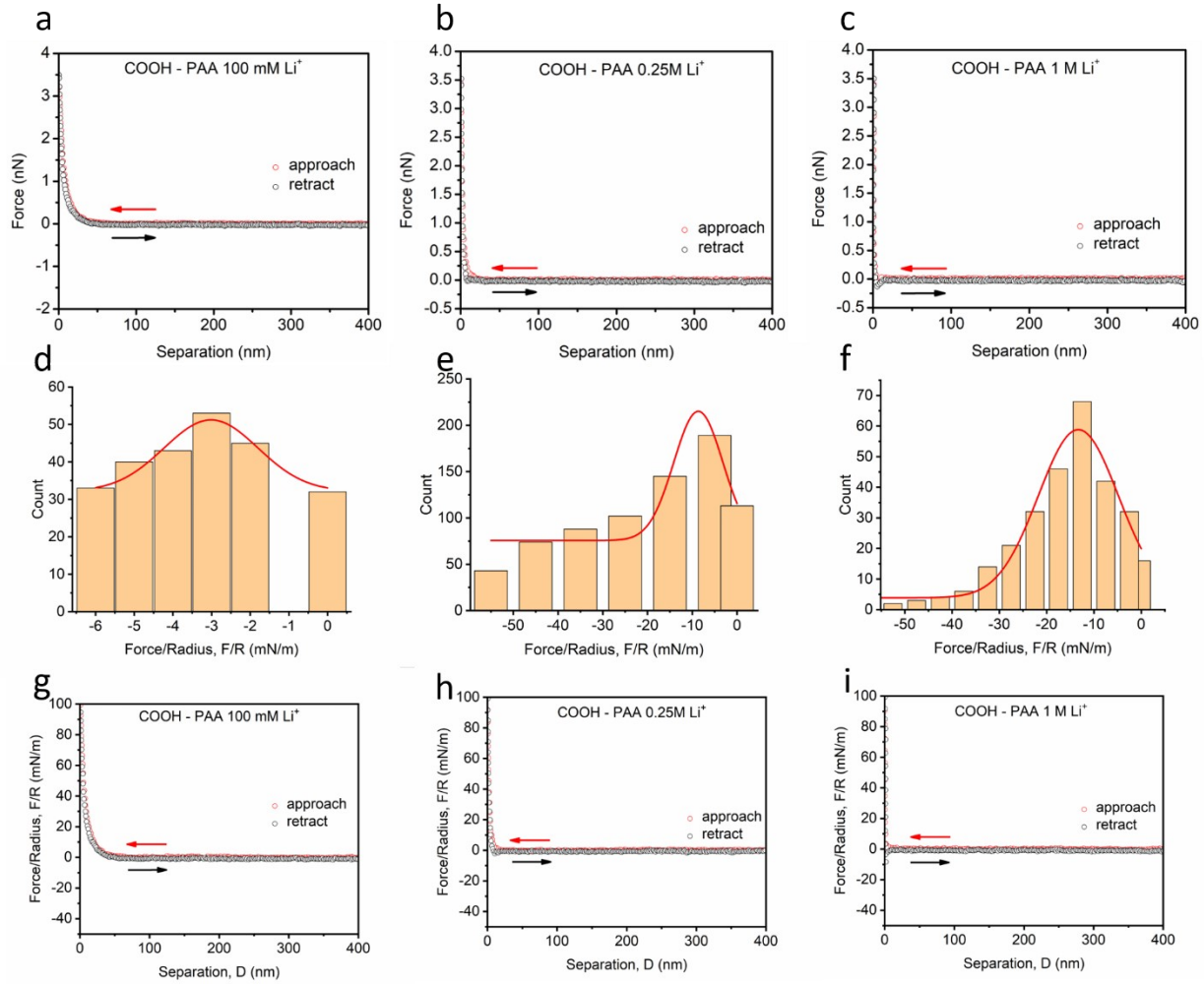

Fig. S20. AFM force measurement between 11-mercaptoundecanoic acid modified tip and Nb_2CTx-PAA covered silica surface in (a) 100 mM Li^+. (b) 0.25 M Li^+. (c) 1 M Li^+. AFM force mapping distribution histogram for 11-mercaptoundecanoic acid modified tip and Nb_2CTx-PAA covered silica surface in (d) 100 mM Li^+. (e) 0.25 M Li^+. (f) 1 M Li^+. Normalized interaction force (Force/tip radius ~30 nm) as a function of separation curve in (g) 100 mM Li^+. (h) 0.25 M Li^+. (i), 1 M Li^+.

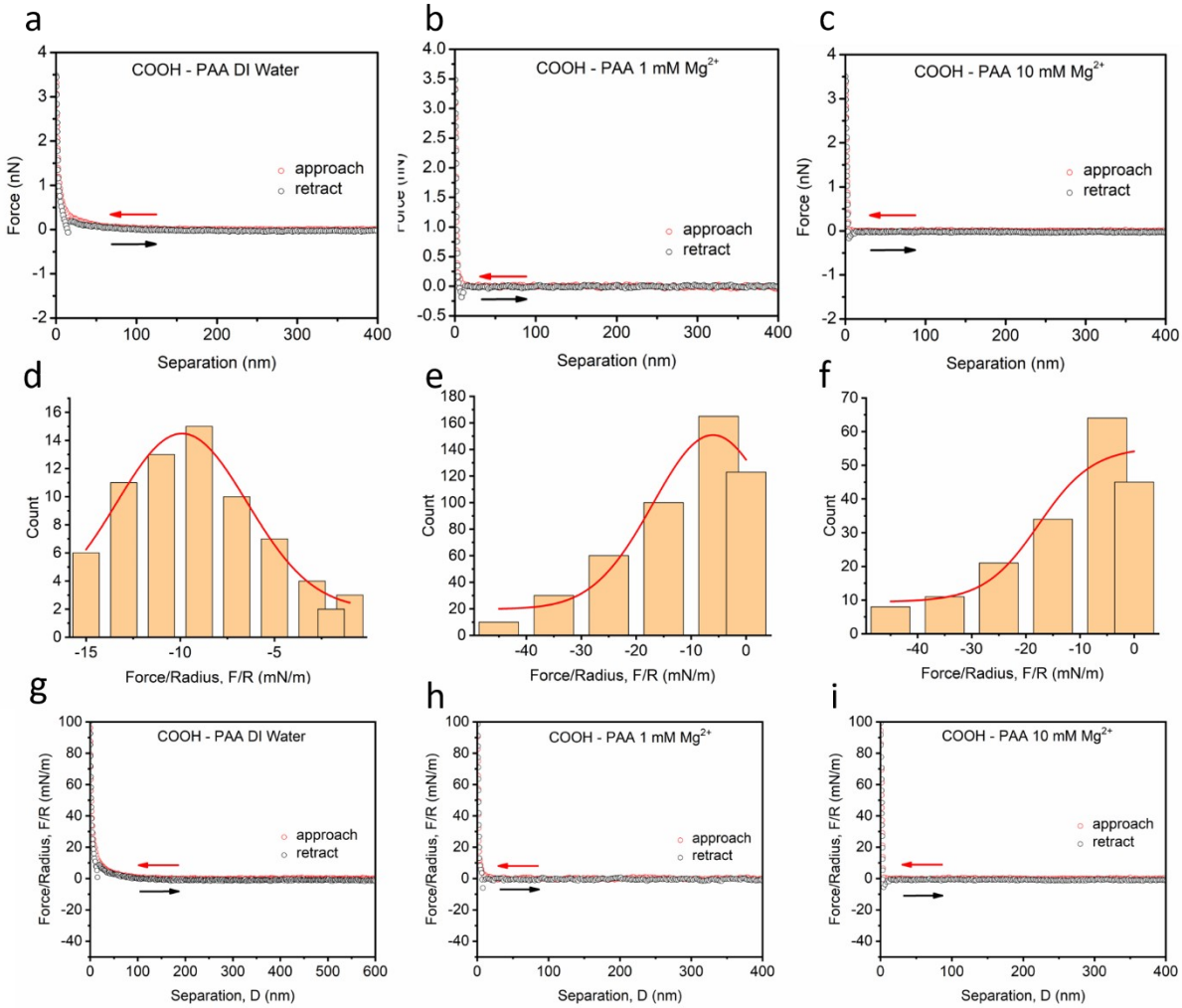

Fig. S21. AFM force measurement between 11-mercaptoundecanoic acid modified tip and Nb_2CTx-PAA covered silica surface in (a) DI water. (b) 1 mM Mg^{2+}. (c) 10 mM Mg^{2+}. AFM force mapping distribution histogram for 11-mercaptoundecanoic acid modified tip and Nb_2CTx-PAA covered silica surface in (d) DI water. (e) 1 mM Mg^{2+}. (f) 10 mM Mg^{2+}. Normalized interaction force (Force/tip radius ~30 nm) as a function of separation curve in (g) DI water. (h) 1 mM Mg^{2+}. (i), 10 mM Mg^{2+}.

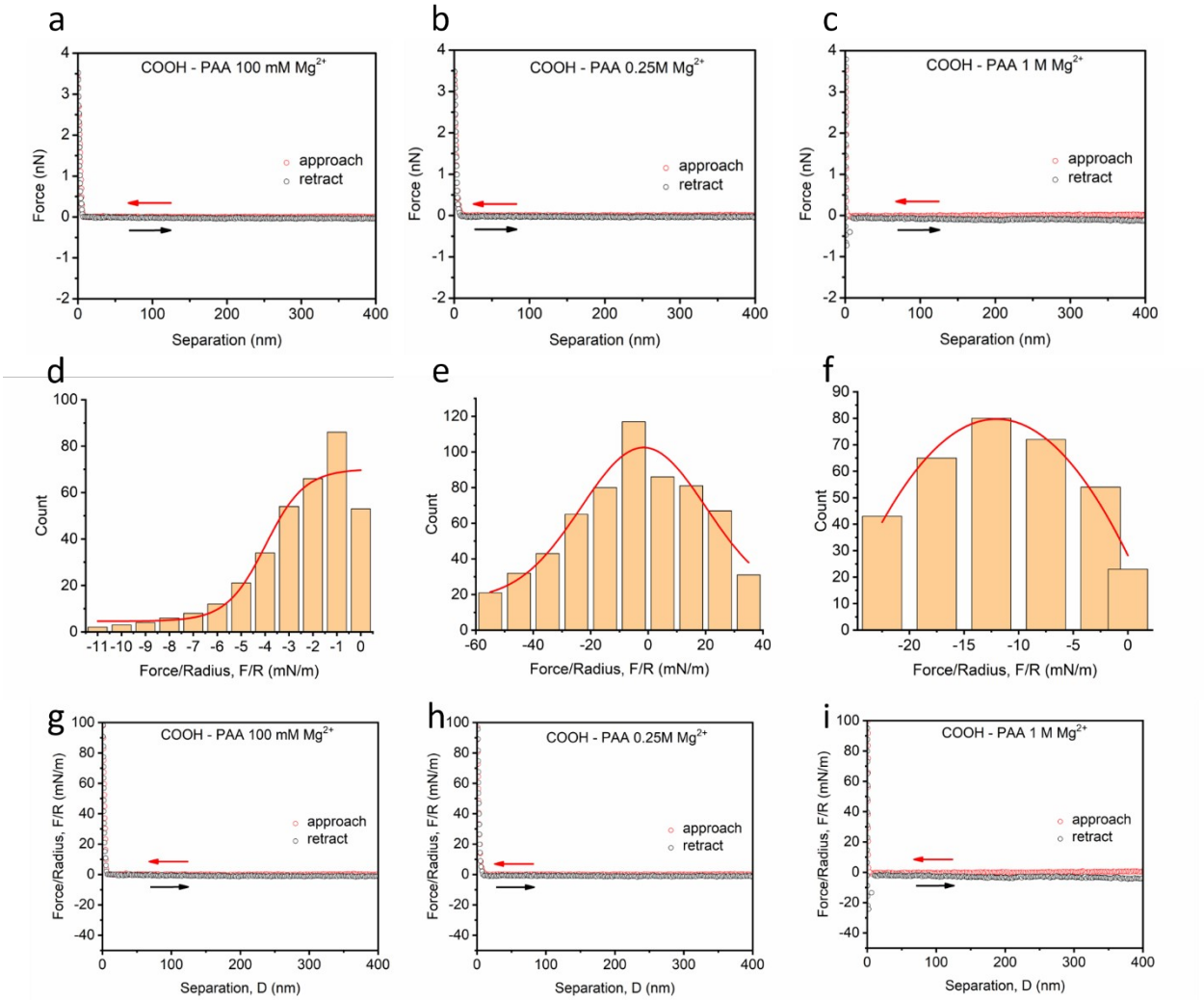

Fig. S22. AFM force measurement between 11-mercaptoundecanoic acid modified tip and Nb_2CTx-PAA covered silica surface in (a) 100 mM Mg^{2+}. (b) 0.25 M Mg^{2+}. (c) 1 M Mg^{2+}. AFM force mapping distribution histogram for 11-mercaptoundecanoic acid modified tip and Nb_2CTx-PAA covered silica surface in (d) 100 mM Mg^{2+}. (e) 0.25 M Mg^{2+}. (f) 1 M Mg^{2+}. Normalized interaction force (Force/tip radius ~30 nm) as a function of separation curve in (g) 100 mM Mg^{2+}. (h) 0.25 M Mg^{2+}. (i) 1 M Mg^{2+}.

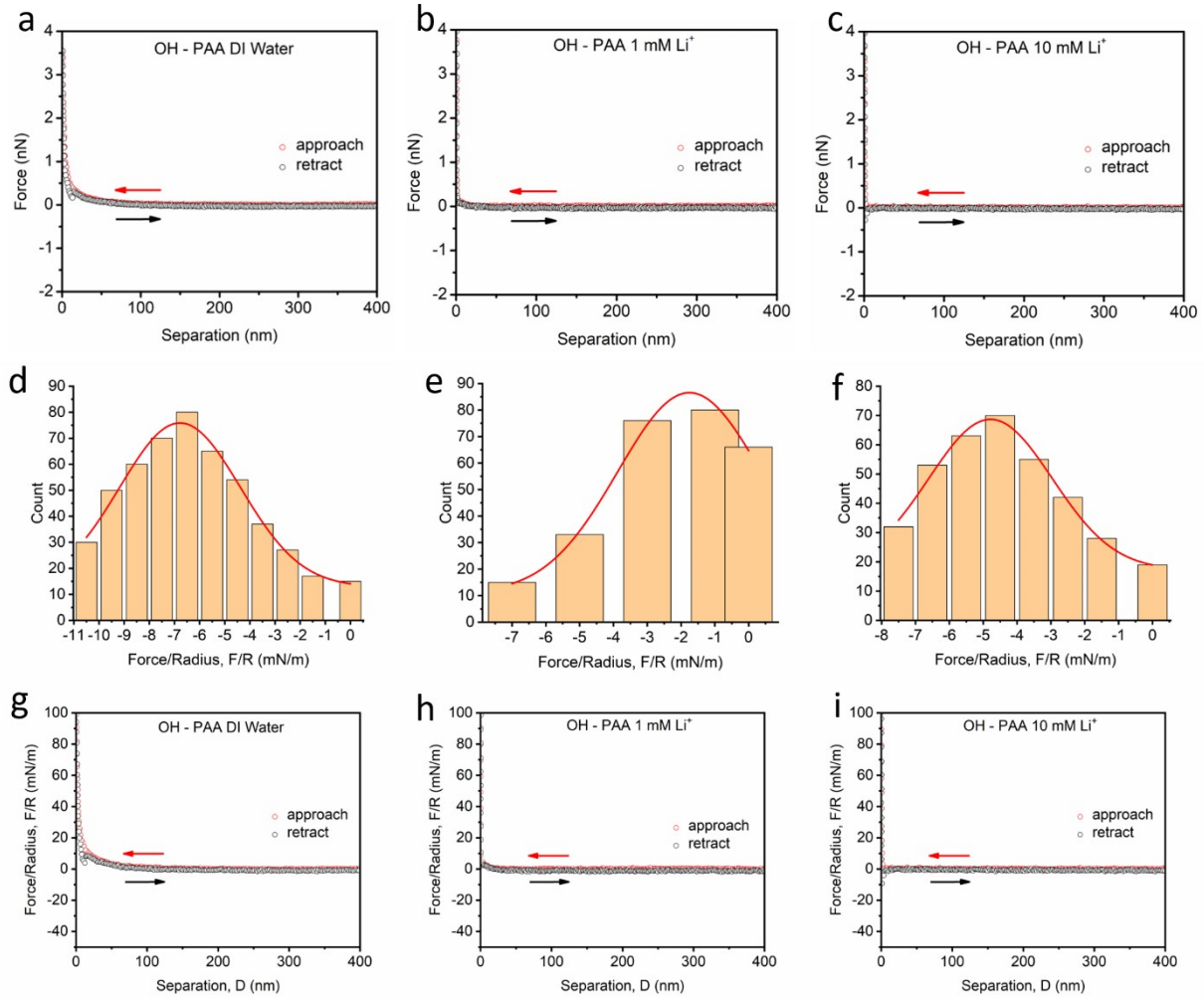

Fig. S23. AFM force measurement between 11-Mercapto-1-undecanol modified tip and Nb_2CTx-PAA covered silica surface in (a) DI water. (b) 1 mM Li^+. (c) 10 mM Li^+. AFM force mapping distribution histogram for 11-Mercapto-1-undecanol modified tip and Nb_2CTx-PAA covered silica surface in (d) DI water. (e) 1 mM Li^+. (f) 10 mM Li^+. Normalized interaction force (Force/tip radius ~30 nm) vs. separation in (g) DI water. (h) 1 mM Li^+. (i) 10 mM Li^+.

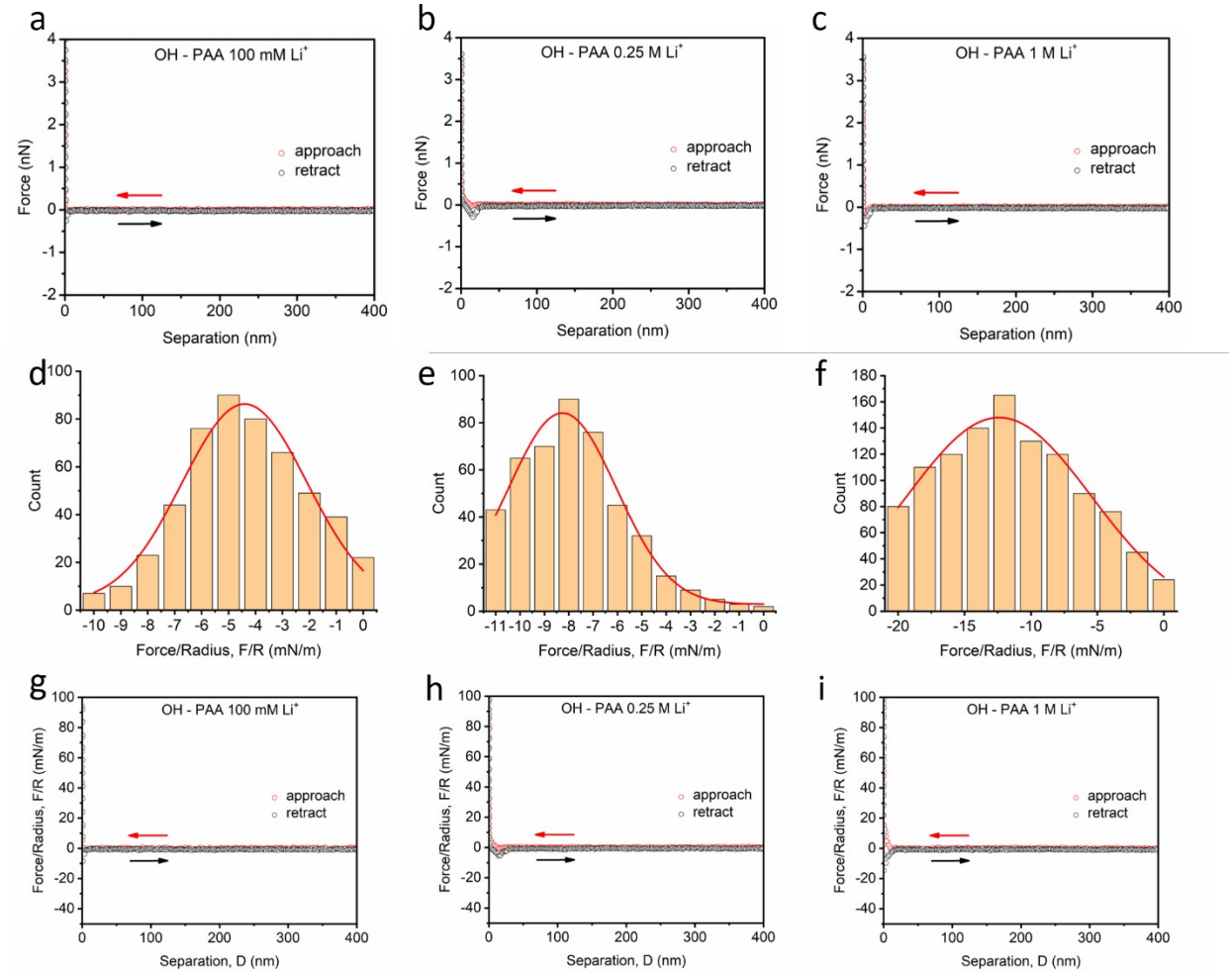

Fig. S24. AFM force measurement between 11-Mercapto-1-undecanol modified tip and Nb_2CTx-PAA covered silica surface in (a) 100 mM Li^+. (b) 0.25 M Li^+. (c) 1 M Li^+. AFM force mapping distribution histogram for 11-Mercapto-1-undecanol modified tip and Nb_2CTx-PAA covered silica surface in (d) 100 mM Li^+. (e) 0.25 M Li^+. (f) 1 M Li^+. Normalized interaction force (Force/tip radius ~30 nm) as a function of separation curve in (g) 100 mM Li^+. (h) 0.25 M Li^+. (i) 1 M Li^+.

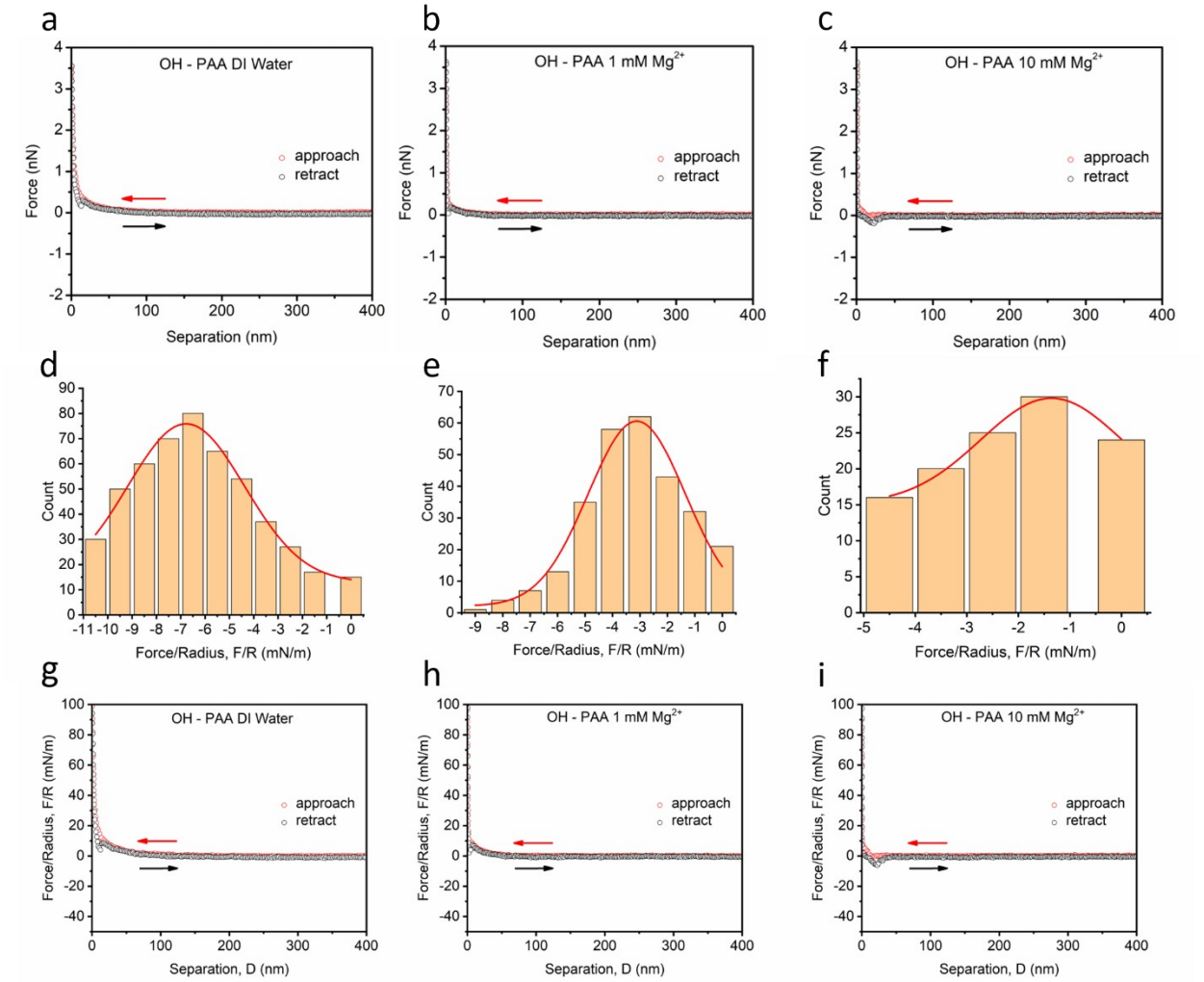

Fig. S25. AFM force measurement between 11-Mercapto-1-undecanol modified tip and Nb_2CTx-PAA covered silica surface in (a), DI water. (b), 1 mM Mg^{2+}. (c), 10 mM Mg^{2+}. AFM force mapping distribution histogram for 11-Mercapto-1-undecanol modified tip and Nb_2CTx-PAA covered silica surface in (d), DI water. (e), 1 mM Mg^{2+}. (f), 10 mM Mg^{2+}. Normalized interaction force (Force/tip radius ~30 nm) as a function of separation curve in (g), DI water. (h), 1 mM Mg^{2+}. (i), 10 mM Mg^{2+}.

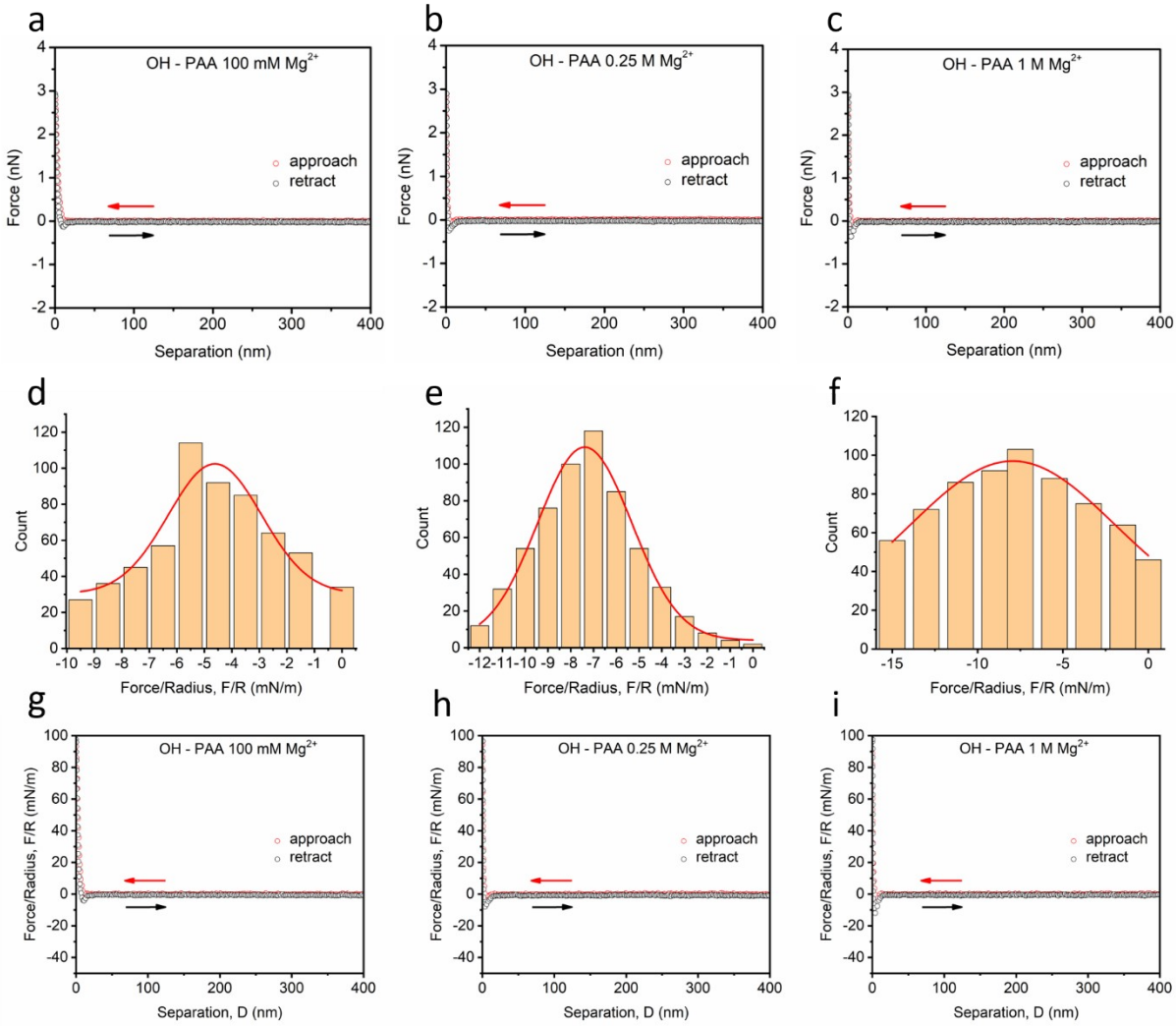

Fig. S26. AFM force measurement between 11-Mercapto-1-undecanol modified tip and Nb_2CTx-PAA covered silica surface in (a), 100 mM Mg^{2+}. (b), 0.25 M Mg^{2+}. (c), 1 M Mg^{2+}. AFM force mapping distribution histogram for 11-Mercapto-1-undecanol modified tip and Nb_2CTx-PAA covered silica surface in (d), 100 mM Mg^{2+}. (e), 0.25 M Mg^{2+}. (f), 1 M Mg^{2+}. Normalized interaction force (Force/tip radius ~30 nm) as a function of separation curve in (g), 100 mM Mg^{2+}. (h), 0.25 M Mg^{2+}. (i), 1 M Mg^{2+}.

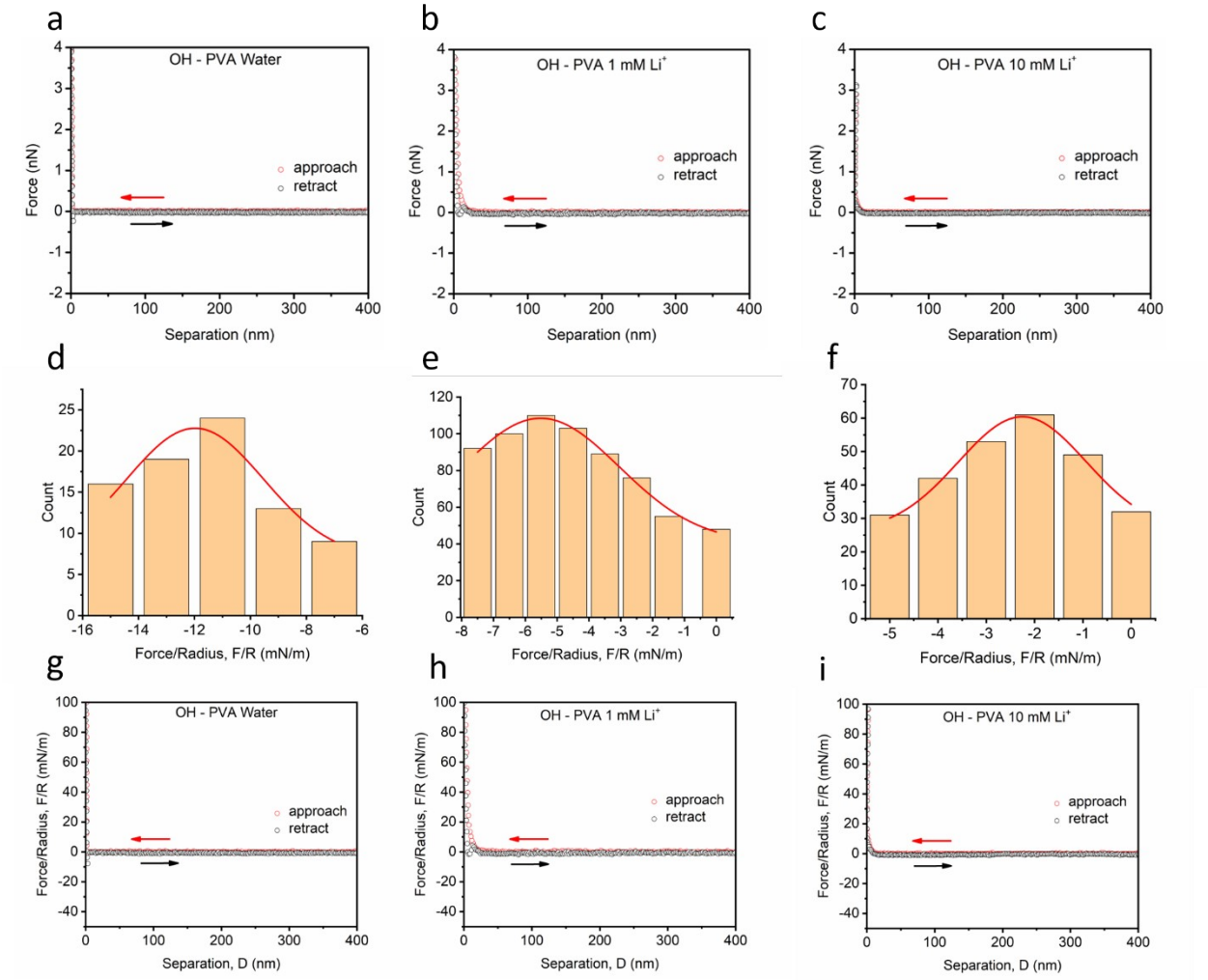

Fig. S27. AFM force measurement between 11-Mercapto-1-undecanol modified tip and Nb_2CTx-PVA covered silica surface in (a), DI water. (b), 1 mM Li^+. (c), 10 mM Li^+. AFM force mapping distribution histogram for 11-Mercapto-1-undecanol modified tip and Nb_2CTx-PVA covered silica surface in (d), DI water. (e), 1 mM Li^+. (f), 10 mM Li^+. Normalized interaction force (Force/tip radius ~30 nm) as a function of separation curve in (g), DI water. (h), 1 mM Li^+. (i), 10 mM Li^+.

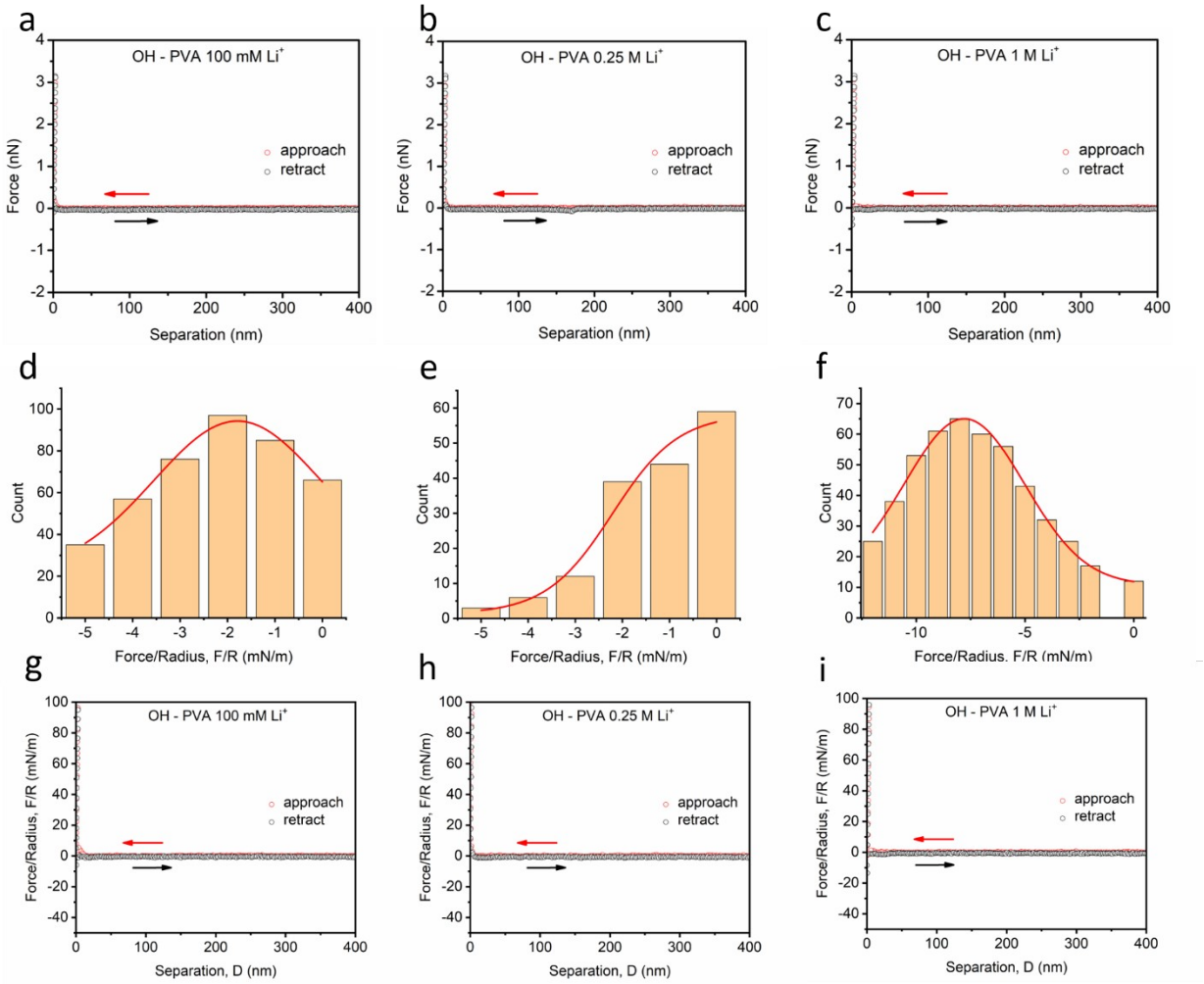

Fig. S28: . AFM force measurement between 11-Mercapto-1-undecanol modified tip and Nb_2CTx-PVA covered silica surface in (a), 100 mM Li^+. (b), 0.25 M Li^+. (c), 1 M Li^+. AFM force mapping distribution histogram for 11-Mercapto-1-undecanol modified tip and Nb_2CTx-PVA covered silica surface in (d), 100 mM Li^+. (e), 0.25 M Li^+. (f), 1 M Li^+. Normalized interaction force (Force/tip radius ~30 nm) as a function of separation curve in (g), 100 mM Li^+. (h), 0.25 M Li^+. (i), 1 M Li^+.

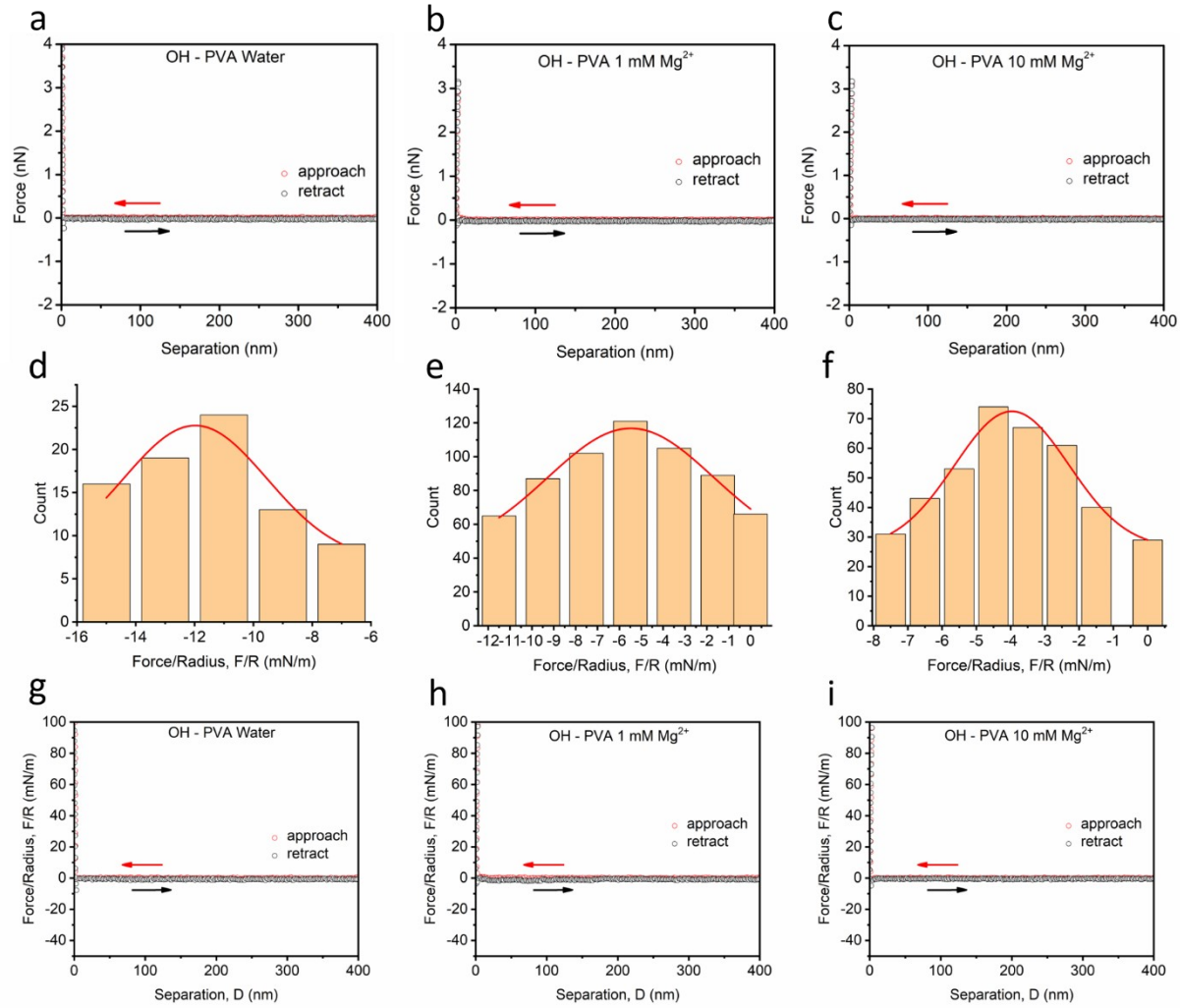

Fig. S29: . AFM force measurement between 11-Mercapto-1-undecanol modified tip and Nb_2CTx-PVA covered silica surface in (a), DI water. (b), 1 mM Mg^{2+}. (c), 10 mM Mg^{2+}. AFM force mapping distribution histogram for 11-Mercapto-1-undecanol modified tip and Nb_2CTx-PVA covered silica surface in (d), DI water. (e), 1 mM Mg^{2+}. (f), 10 mM Mg^{2+}. Normalized interaction force (Force/tip radius ~30 nm) as a function of separation curve in (g), DI water. (h), 1 mM Mg^{2+}. (i), 10 mM Mg^{2+}.

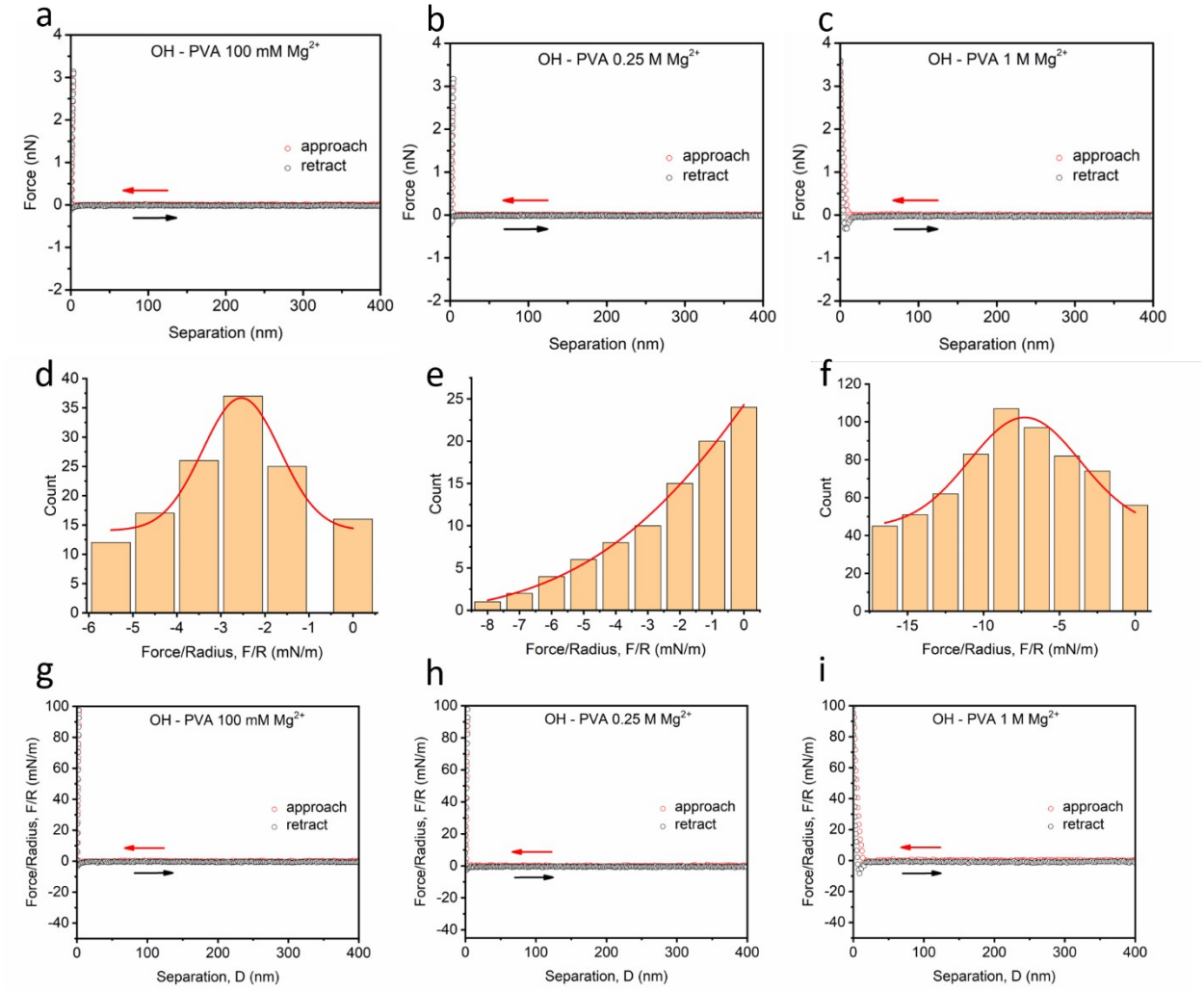

Fig. S30. AFM force measurement between 11-Mercapto-1-undecanol modified tip and Nb_2CTx-PVA covered silica surface in (a) 100 mM Mg^{2+}. (b) 0.25 M Mg^{2+}. (c) 1 M Mg^{2+}. AFM force mapping distribution histogram for 11-Mercapto-1-undecanol modified tip and Nb_2CTx-PVA covered silica surface in (d) 100 mM Mg^{2+}. (e) 0.25 M Mg^{2+}. (f) 1 M Mg^{2+}. Normalized interaction force (Force/tip radius ~30 nm) as a function of separation curve in (g) 100 mM Mg^{2+}. (h) 0.25 M Mg^{2+}. (i), 1 M Mg^{2+}.

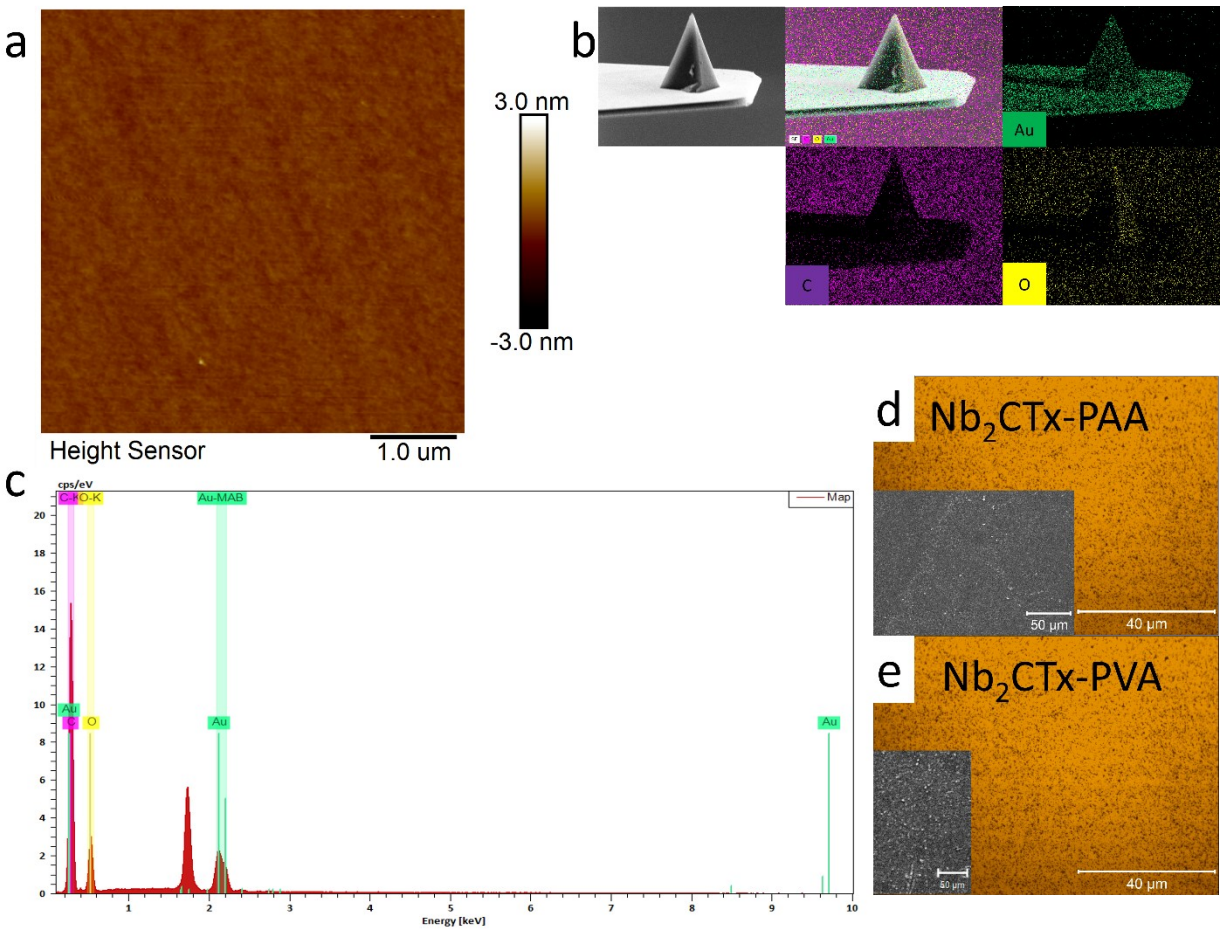

Fig. S31. Sample surface and AFM tip characterization: (a) flat height profile for silica. (b) and (c) EDX mapping and element profile for either 11-Mercapto-1-undecanol or 11-mercaptoundecanoic acid modified tip (cross section area). (d) optical image for Nb_2CTx-PAA modified silica surface. (e) optical image for Nb_2CTx-PVA modified silica surface.

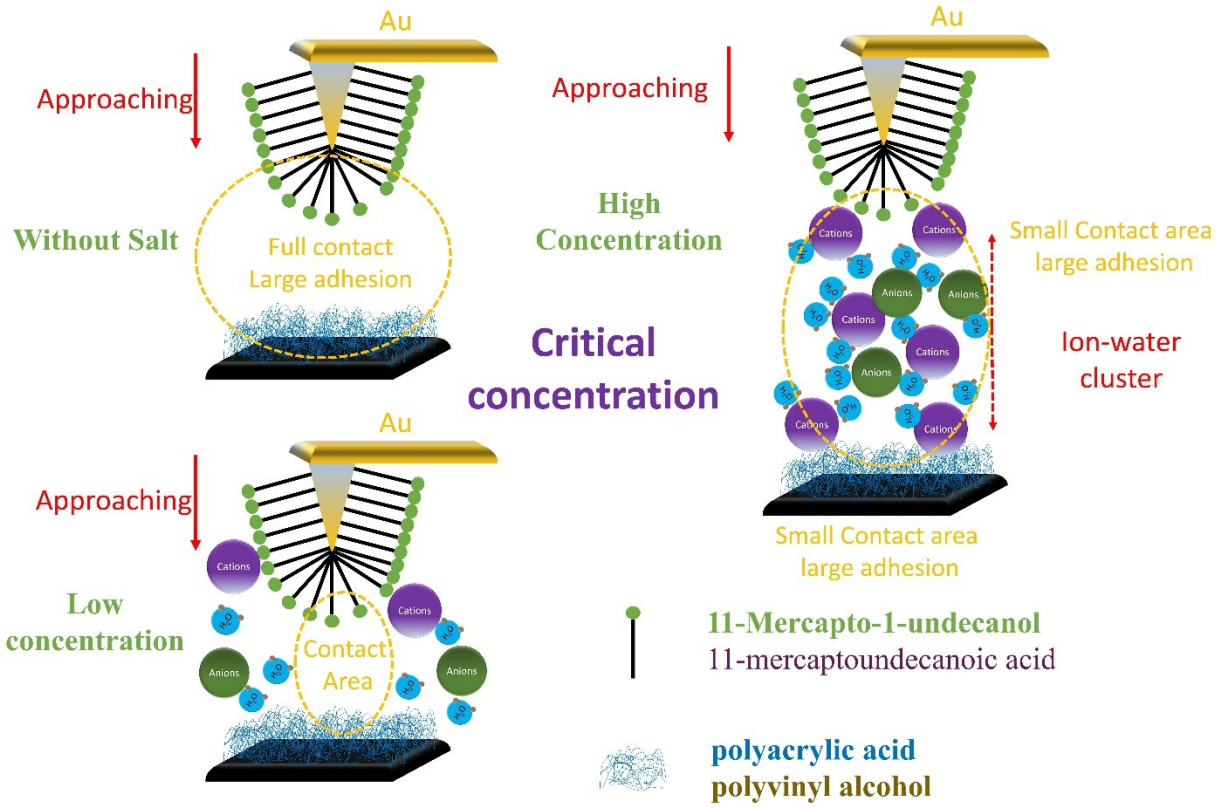

Fig. S32. Schematic illustration on possible effect (or interaction mechanism） of ion/water cluster on AFM force measurements between functionalized tip and substrate surface.

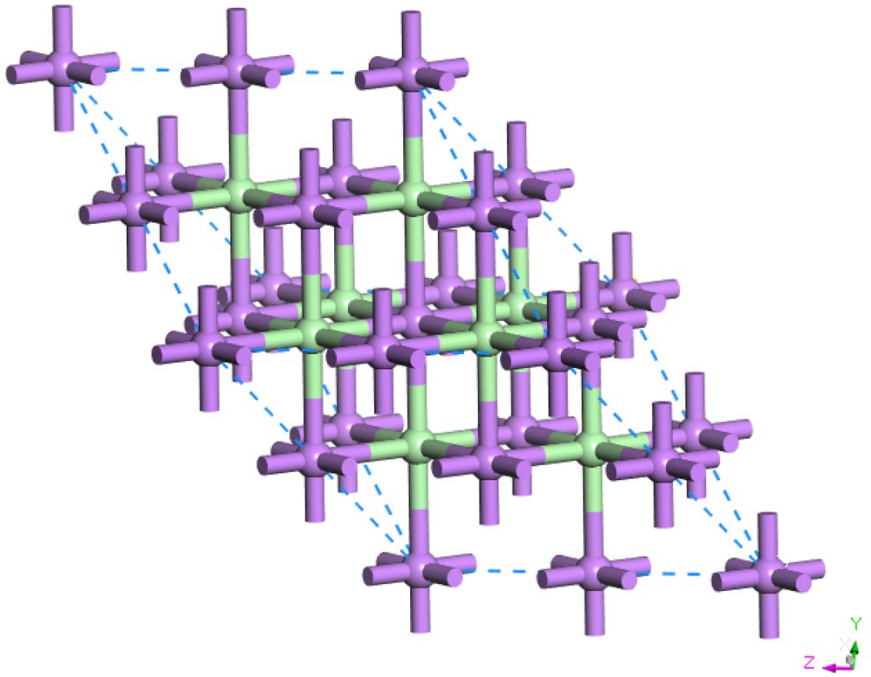

Fig. S33. The crystal structure of LiCl (Hermann Mauguin: Fm3m [225]; Hall: -F 4 2 3; Point Group:m3m; Crystal System: cubic).

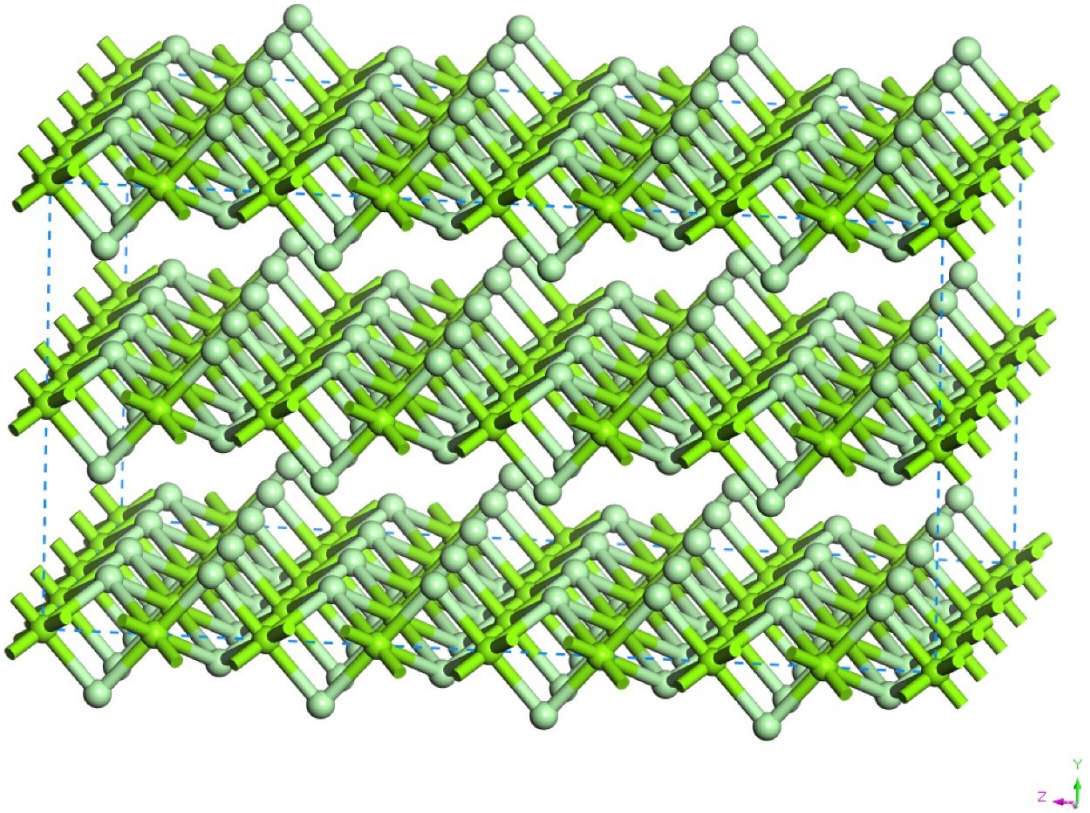

Fig. S34. The crystal structure of $MgCl_2$ (Hermann Mauguin: Pmma [51]; Hall:-P 2a 2a; Point Group: mmm; Crystal System: orthorhombic).

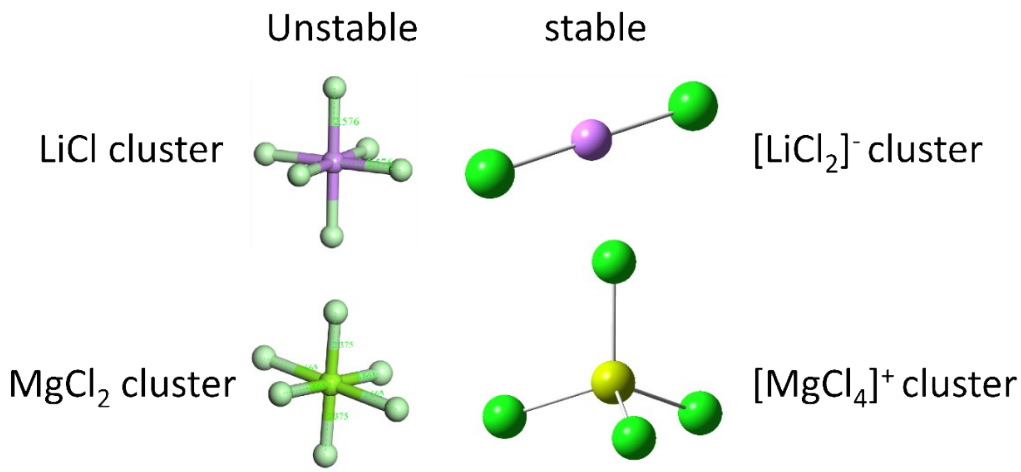

Fig. S35. Computational models of LiCl and $MgCl_2$ cluster: The calculation results demonstrate conventional LiCl and $MgCl_2$ cluster are not stable, the stable structures for LiCl and $MgCl_2$ are $[LiCl_2]^-$ and $[MgCl_4]^+$ cluster as shown in the above figure.

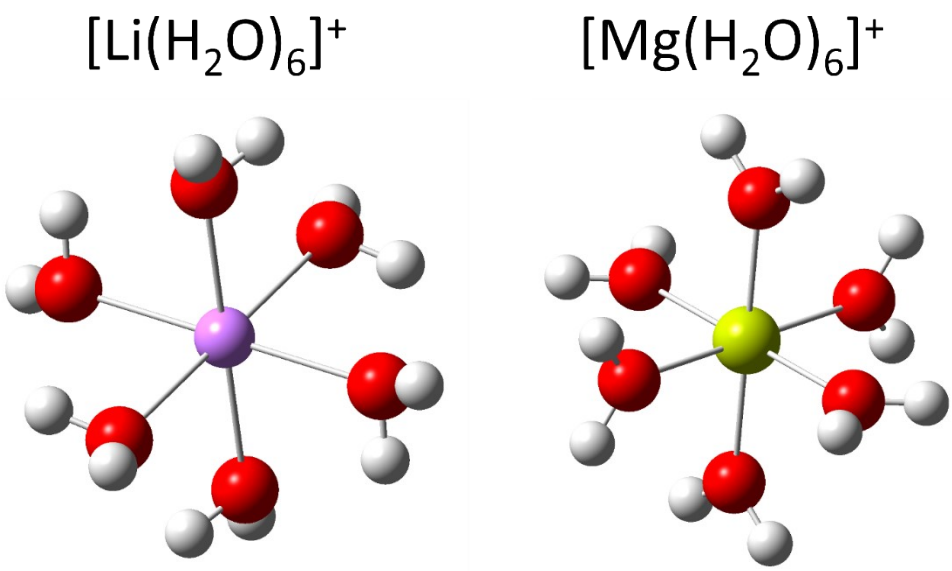

Fig. S36. Computational models of hydrated Li and Mg ions.

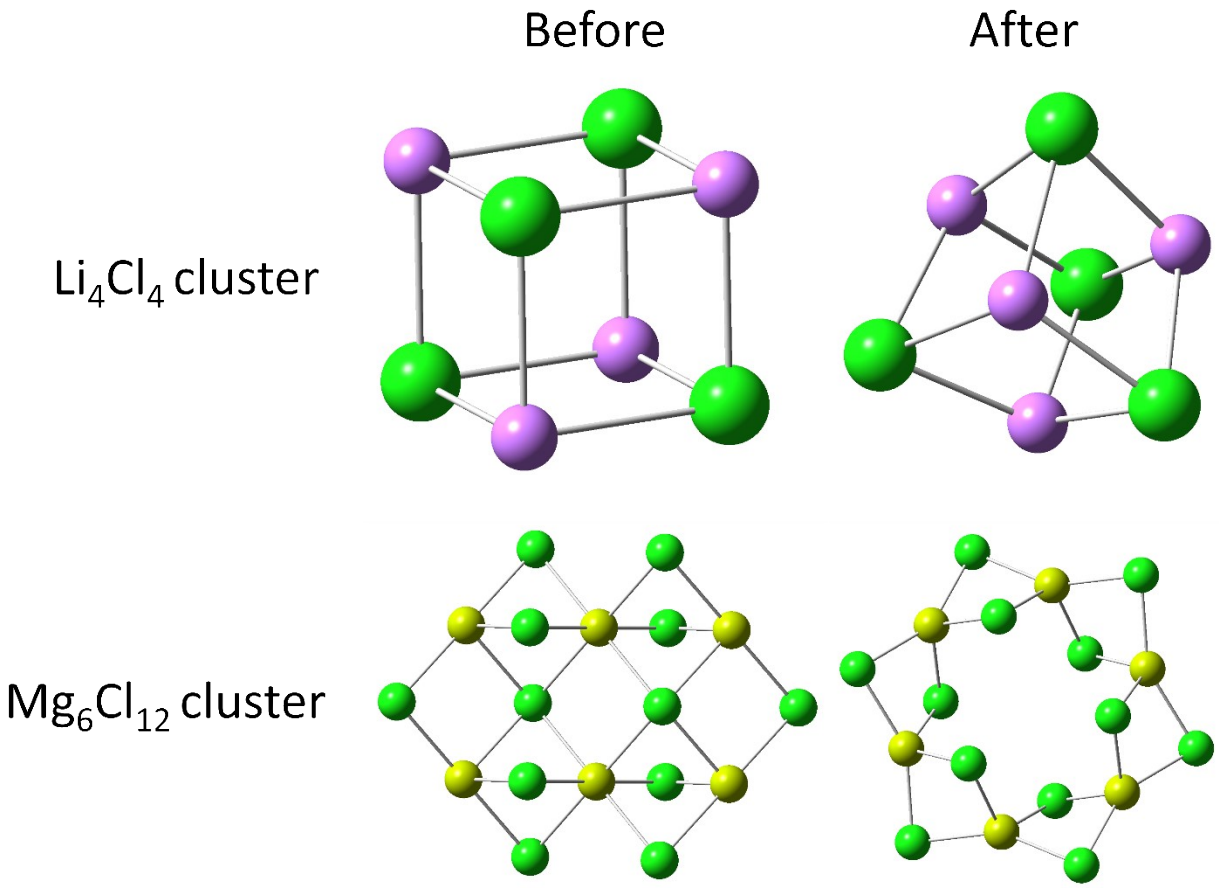

Fig. S37. Optimized stable structure of $[LiCl_2]^-$ and $[MgCl_4]^+$ cluster: The most stable cluster from computational method for LiCl and $MgCl_2$ are Li_4Cl_4 and Mg_6Cl_{12} (left). The optimized structure of both Li_4Cl_4 and Mg_6Cl_{12} cluster are shown on the right.

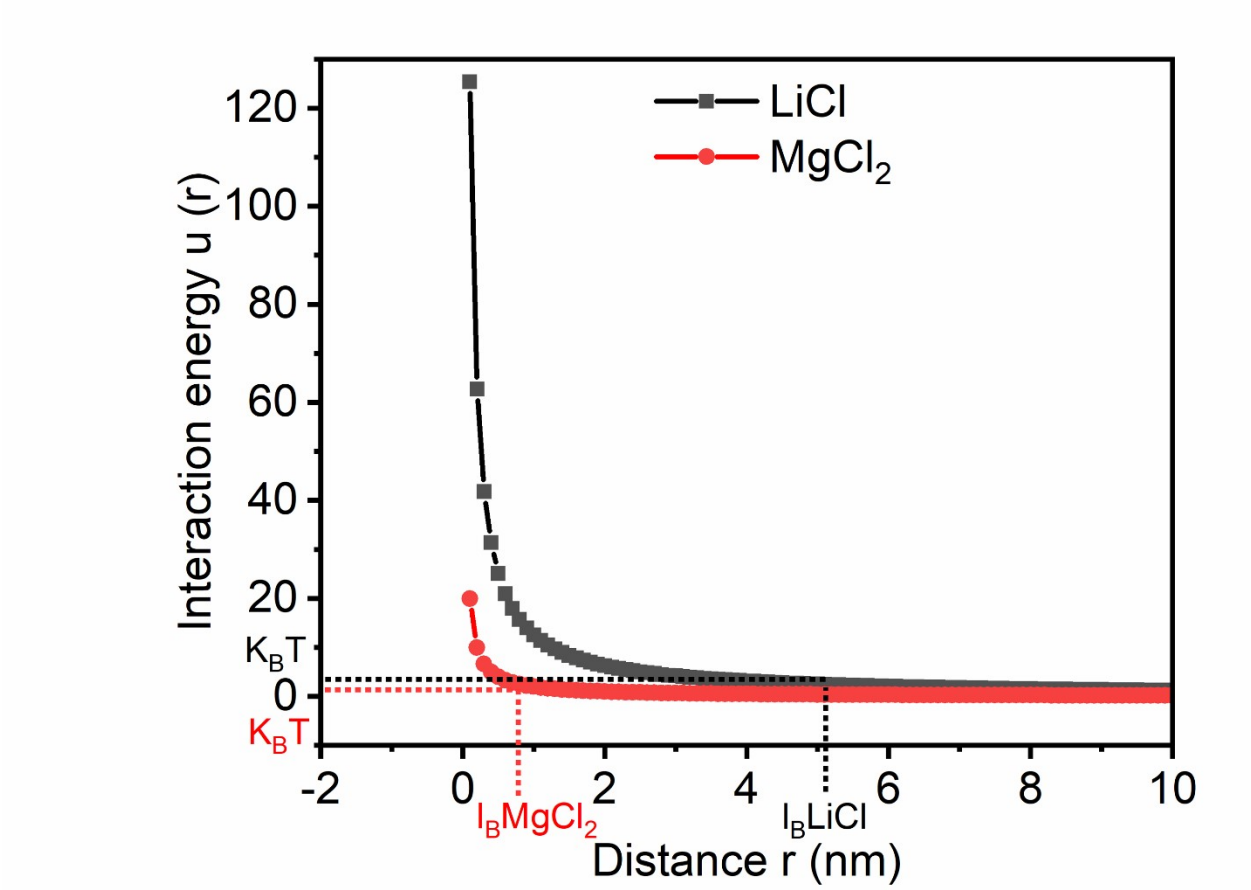

Fig.S38. Ion pair energy calculated by using *Bjerrum length* l_B.

Supplementary References

1 Israelachvili, J. N. in *Intermolecular and Surface Forces (Third Edition)* (ed Jacob N. Israelachvili) 71-90 (Academic Press, 2011).

2 Parkhurst, D. L., and Appelo, C.A.J., . Description of input and examples for PHREEQC version 3—A computer program for speciation, batch-reaction, one-dimensional transport, and inverse geochemical calculations. *U.S. Geological Survey Techniques and Methods* **6**, 497, doi:https://pubs.usgs.gov/tm/06/a43/ (2013).

3 Dill, K. A., Bromberg, S. & Stigter, D. *Molecular Driving Forces: Statistical Thermodynamics in Chemistry and Biology*. (Garland Science, 2003).

4 Einarsrud, M. A., Justnes, H., Rytter, E. & Øye, H. A. Structure and stability of solid and molten complexes in the MgCl2-AlCl3 system. *Polyhedron* **6**, 975-986, doi:https://doi.org/10.1016/S0277-5387(00)80942-0 (1987).

5 Marshall, B. J., Pederson, D. O. & Dorris, G. G. Elastic constants of LiCl and RbCl from 300°K to 4.2°K. *Journal of Physics and Chemistry of Solids* **28**, 1061-1067, doi:https://doi.org/10.1016/0022-3697(67)90223-5 (1967).